1-1-2011

Development of a novel automated micro-assembly mechanism

Yuan Xue
Ryerson University

DEVELOPMENT OF A NOVEL AUTOMATED MICRO-ASSEMBLY MECHANISM

by

Yuan Xue

Bachelor of Engineering, Ryerson University, 2009

A thesis

presented to Ryerson University

in partial fulfillment of the

requirements for the degree of

Master of Applied Science

in the Program of

Mechanical Engineering

Toronto, Ontario, Canada, 2011

Author's declaration

I hereby declare that I am the sole author of this thesis.

I authorize Ryerson University to lend this thesis or dissertation to other institutions or individuals for the purpose of scholarly research.

_____

Yuan Xue

I further authorize Ryerson University to reproduce this thesis by photocopying or by other means, in total or in part, at the request of other institutions or individuals for the purpose of scholarly research.

_____

Yuan Xue

Title of thesis: Development of a novel automated micro-assembly mechanism

Name: Yuan Xue

Master of Applied Science in the Program of Mechanical Engineering, Ryerson of University, 2011

Abstract

In this thesis a novel automated micro assembly mechanism is developed. The assembly mechanism utilizes repulsive-force actuators to flip surface-micromachined 2D structures out-of-plane and assemble them into 3D micro devices. The novel micro assembly mechanism is suitable for wafer-level multi-devices batch assembly without external interference. It can assemble 2D structures not only at the vertical position (perpendicular to the substrate) but also at positions at any angle to the substrate. Two approaches, i.e., graphic method and analytical method, are proposed for designing the micro assembly mechanism. Prototypes are fabricated using the PolyMUMPs surface micromachining technology and tested. The experimental results verify the concept of the novel automated micro assembly mechanism. The strength of the assembled 3D structures in terms of withstanding external acceleration is calculated. The calculated result well matches the experimental result which is about 7g. Using the micro assembly mechanism, 1D and 2D rotation micromirrors are designed for various applications.

Acknowledgements

I would like to thank:

Table of Contents

List of Figures

List of Tables

x

Chapter 1 Introduction

1.1 MEMS

Micro-electro-mechanical Systems (MEMS) are micro scale mechanical and electrical elements integrated on the same chip using microfabrication techniques. MEMS have the advantages of small size ranging from less than 1 micron to several millimetres [1], high integration, low cost, and high reliability. MEMS technology has been widely used in many industry fields from auto industry, aerospace, medical and health care to communication and consumer electronics. Typical MEMS can be categorized as sensor and actuator based micro devices. The sensors (Figure1-1a) can measure acceleration, pressure, temperature, magnetic fields, vibration, rotation, etc. The actuators are used in micro-mirrors (Figure1-1b), micro-ratcheting-actuator (Figure1-1c), micro-resonator (Figure1-1d), VOA (variable optical attenuator) (Figure1-1e), micro-switches (Figure1-1f), micro-valves, micro-pumps, and others [1].

1.2 MEMS manufacturing technology

MEMS devices, which could integrate micro-sensors, micro-actuators along with integrated circuits (IC), are normally fabricated on silicon chips. The electronics are fabricated using integrated circuit process techniques (e.g. CMOS, Bipolar, or BICMOS processes), while the micromechanical components are fabricated using micro-machining techniques to selectively etch the silicon wafer away or add new structural layers [1]. The micromachining has several major steps: film deposition, doping, lithography, etching, dicing, and packaging [2] [3].

- Film deposition: Starting with a silicon wafer as the substrate, one or more thin films are deposited. Depending on device types, the deposition technique can be thermal oxidation, chemical vapor deposition (CVD), physical vapor deposition (PVD), or epitaxy.

- Material doping: Impurity may be introduced into the layer for various purposes, such as changing conductivity, forming etching stop layer, etc. Doping can be done by thermal diffusion or ion implantation.

- Patterning: A pattern is transferred to the film using mask to form required features. The process of pattern generation and transfer is called photolithography.
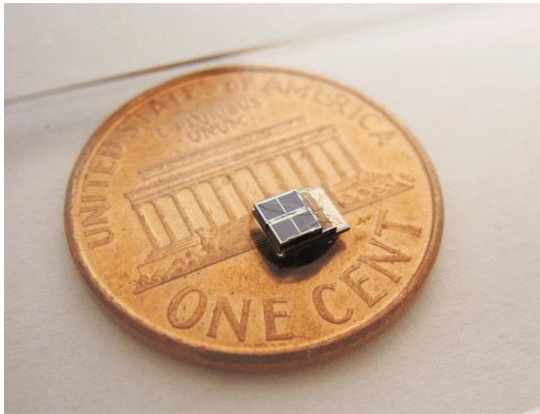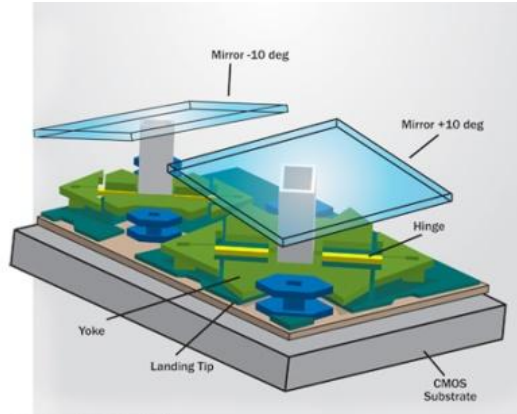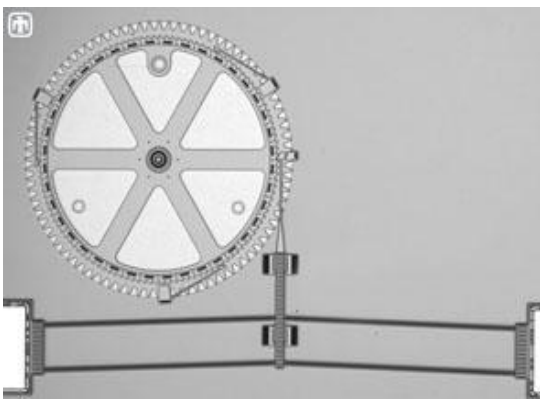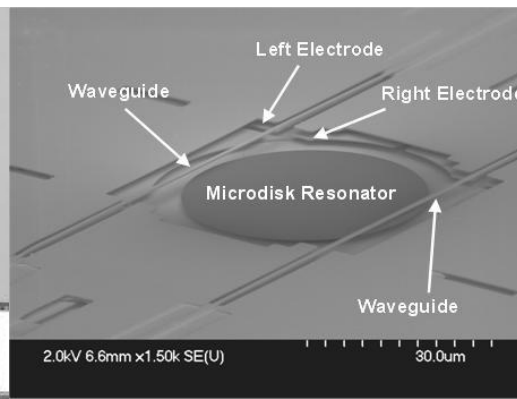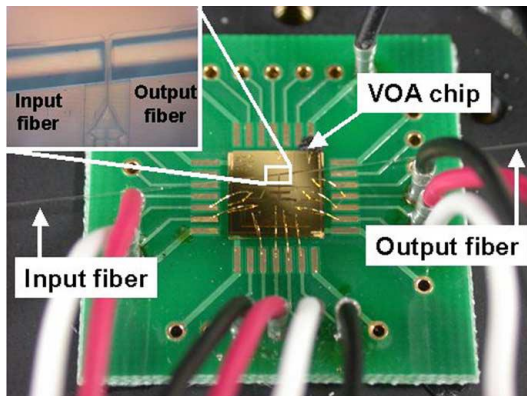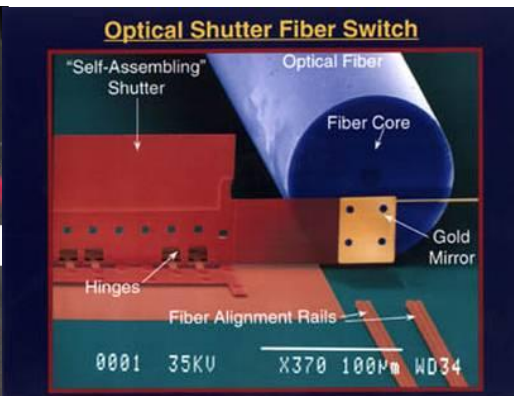
Figure 1-1: MEMS devices (a) Micro Sensor [4], (b) Micromirror [5], (c) Thermal Ratcheting Actuator [6], (d) Micro Resonator [7], (e) MEMS VOA [8], (f) MEMS optical switch [9]

- Etching: Etching is the selective removal of unwanted regions of a film or substrate. Etching techniques include wet etching (chemical etching) and dry etching (plasma etching), such as reactive ion etching (RIE) or Deep RIE.

- Dicing: The finished wafer is diced into small pieces, from which electronic components can be made.

- Packaging: Packaging is performed to connect and protect the individual units.

There are two types of manufacturing processes: bulk micromachining and surface micromachining.

Bulk micromachining is normally used for silicon based MEMS manufacturing. It produces structures by selectively etching inside a substrate [10], which is usually a silicon wafer. The etching process starts with transferring a pattern from a mask to the surface by photolithography. Anisotropically wet etching is usually done on the silicon wafer with alkaline liquid solvents, such as potassium hydroxide (KOH) or tetramethylammonium hydroxide (TMAH). These solutions have a very low etching rate in certain direction on the (111) crystal face, which permits formation of distinct geometric structures with sharp edges and precise dimensions. The fabricated substrate can be bonded to form needed shapes.

Surface micromachining builds microstructures by adding and etching different structural layers on top of the substrate [11]. Polysilicon is usually used as the structural layers and silicon dioxide is used as a sacrificial layer. Each layer is patterned by photolithography and subsequently selectively etched by either a wet etch or a dry etch. Wet etch uses an acid and dry etching can combine chemical etching with physical etching like ionized gas or plasma. The sacrificial layer is removed during the fabrication process to create the necessary space in the thickness direction, using a selective etch process that will not damage the structural layer.

These two types of MEMS manufacturing technologies have their own characteristics and are suitable for different applications. Surface micromachining enables the fabrication of complex systems with multiple electronic and mechanical components on the same substrate. The surface micromachined components are on the top but not inside of substrate, therefore the substrate is not necessary to be silicon wafer. It can be substituted by cheaper substrates, such as glass or plastic, and can be larger, not restricted by the size of silicon wafer. Furthermore, the structures manufactured by surface micromachining are smaller compared to those by the bulk micromachining.

Bulk micromachining is suitable to fabricate 3D structures. But the fabricated structures are relatively simple and the fabrication cost is high. Surface micromachining can fabricate only 2D planar structures. But complex micro structures can be fabricated and the cost is low due to the process is very similar to well developed IC industry processes. In order to fabricate 3D micro structures of complex shape with low cost, micro assembly technology has been developed, which assembles surface-micromachined 2D structures into 3D devices.

1.3 Literature Review

1.3.1 Micro-assembly

Micro-assembly
- Non-automated
  - Manually manipulation
  - Robotics manipulation
- Automated
  - Centrifugal force
  - Magnetic force
  - Residual stress
  - Thermokinectic
  - Electrostatic (Ultrasonic Vibration)
  - Liquid
  - Chemical
  - Template
  - Thermal Actuators
  - Scratch drive
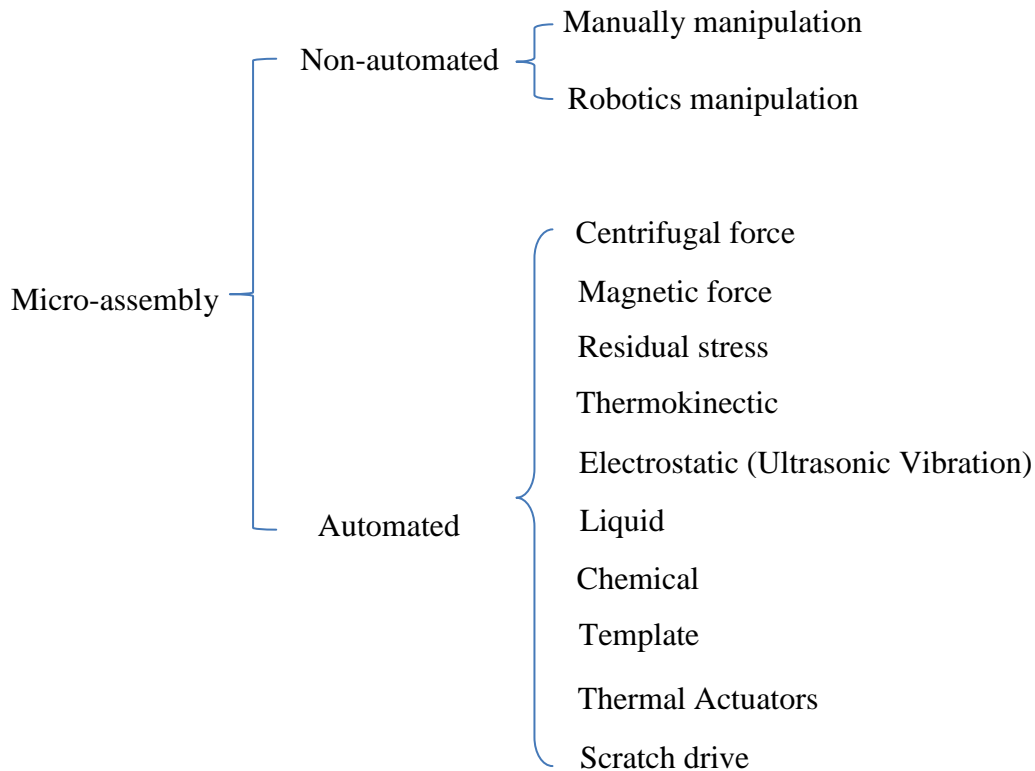
Figure 1-2: Categories of auto-assembly techniques

Various assembly techniques have been proposed and investigated in recent years. Basing on their assembly processes, these assemblies can be categorized to non-automated and automated, as indicated in Figure 1-2. Assemblies requiring external mechanical contact to the assembled parts such as using a probe either manually or by robotics are considered as non-automated. This method cannot realize batch production and lead to a low efficiency. In contrast, automated

4

assembly techniques can complete the assembly process automatically and achieve high efficiency wafer-level batch production without any mechanical intervention from outside of chips.

1.3.1.1 Non-automated assemblies

Non-automated assemblies include manual [12] [13] [14] [15] [16] and robotic [17] [18] probe manipulation. Probes, which are usually made by tungsten, have been widely used to assemble microstructures. Most probe manipulations are manual processes. In order to realize automatic assembly, robotics probe manipulation techniques have been developed, e.g. a parallel 6-DOF robot manipulator as shown in Figure 1-3 [17]. The manipulation can be parallel if multiple microgrippers are connected to the probe and work at the same time; otherwise, it is a serial assembly. The robotics probe manipulation is simple and flexible, but its disadvantages are also significant. The number of structures that can be assembled simultaneously by parallel assembly is limited. For example, the manipulator having three grippers in [17] is able to operator on three targets at the same time. However, the alignment of grippers is a problem which affects the success rate for assembly. Since they cannot be used in batch production, manual and robotic probe assemblies are not considered as automated processes.

1.3.1.2 Automated assemblies

Automated assembly techniques can achieve batch assembly on structures within the same wafer, without the requirement of any external mechanical intervention from outside of chips.

Centrifugal force based auto-assembly uses a rotation system (as shown in Figure 1-4) to generate centrifugal force [19] [20]. The chip containing the microstructures is attached to a rotating disk perpendicularly to the rotating axis with the micromachined surface facing outward. When the centrifugal force is large enough to overcome friction or surface forces, the top plate rotates outward. The plate is then locked by a locking system at the desired angle. This mechanism has many advantages over conventional assembling methods. It is a fast, low-cost, non-contact, and high-yield batch assembly technique, but only the structures with the same design can be assembled simultaneously by centrifugal force.
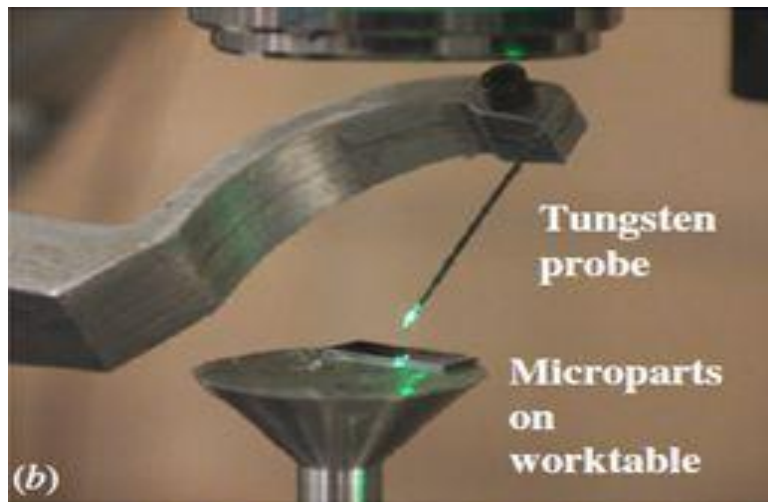
(a)
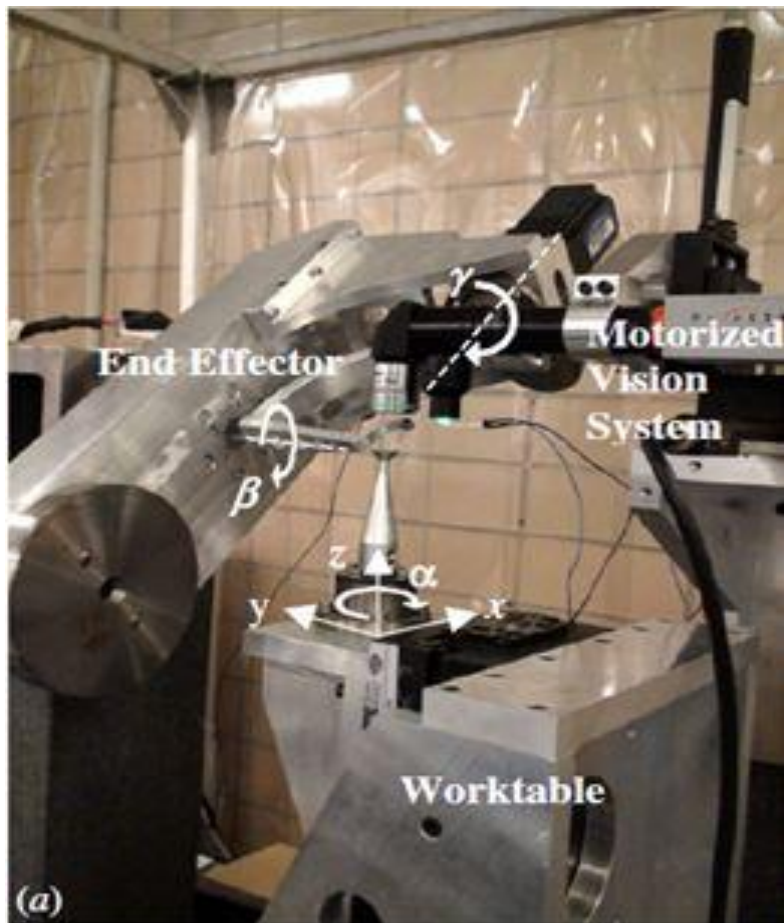
(b)

Figure 1-3: Probe manipulation (a) the magnified view of the MEMS micropart, worktable and tungsten probe, (b) 6-DOF manipulator [17]
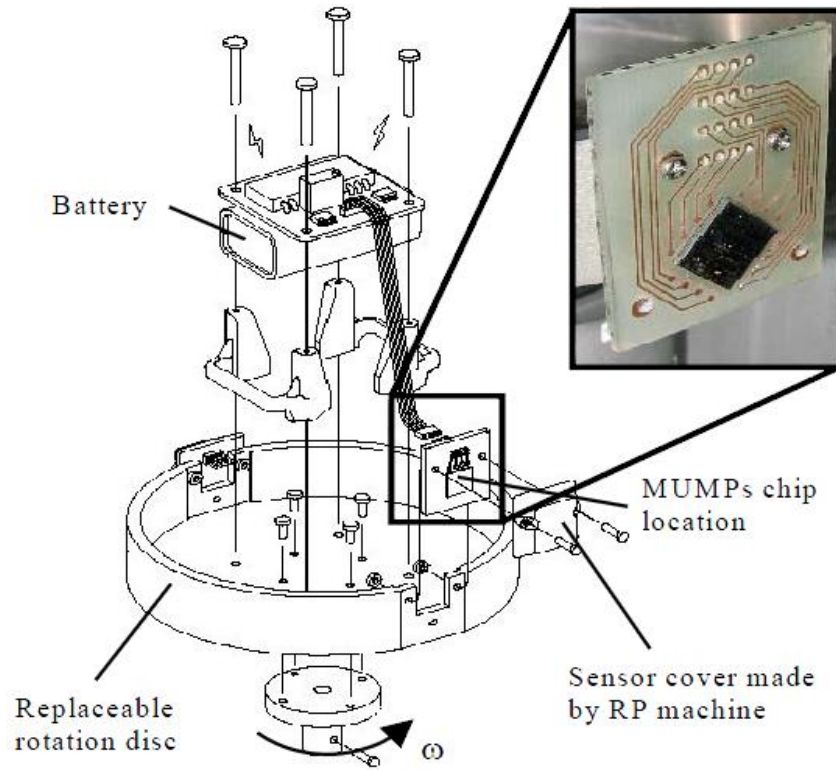
Figure 1-4: Conceptual drawing of the centrifugal assembling setup [20]
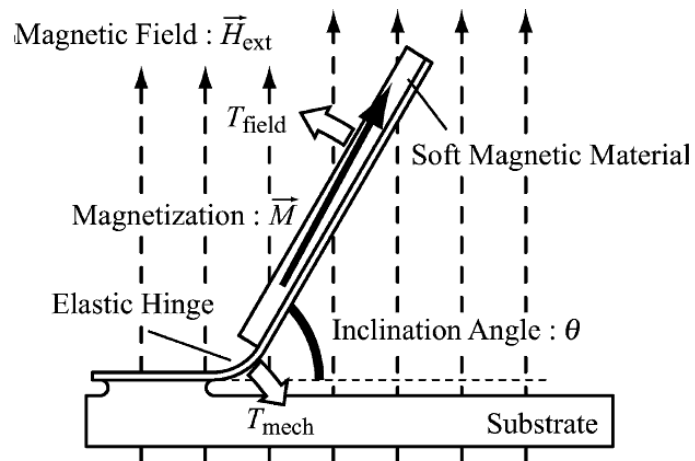
Figure 1-5: Direction of torque acting on hinged structure in magnetic field [21]
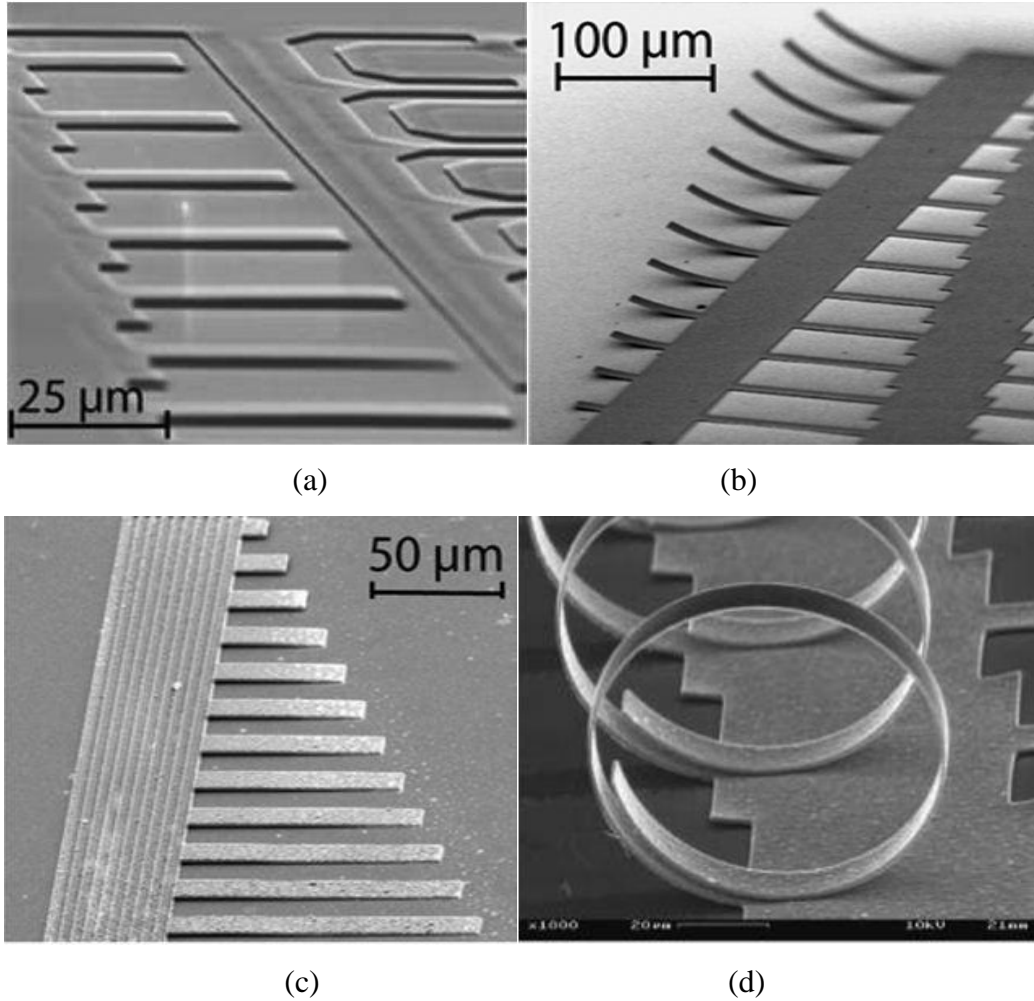
Figure 1-6: Released cantilevers using stress: (a) Si, (b) Si –Si3N4, and (c) Si – Si3N4 Al before, and (d) after RTA at 600 C for 120s [22]

Magnetic force is another important method of auto-assembly [21]. In magnetic force assembly, an external magnetic field is applied perpendicular to the substrate, which generates a torque to lift the hinged structures as shown in Figure 1-5. However, a large number of micro-structures are made of silicons or polysilicons, which are not magnetic materials. To make the magnetic force effective, a metal layer has to be deposited on structure or the structure need be made by magnetic materials (e.g., nickel, iron, or cobalt), that increase the cost of processing.

Stress is also used for self-assembly (see Figure 1-6) [22]. Internal stress usually exists in multilayered structures caused by the different thermal expansion rate of each layer. By control this internal stress and the plastic yielding of a metallic layer, the surface machined micro-structure is able to form three-dimensional.

The thermokinetic force is generated by the energetic gas molecules emanating from the heated substrate, which increases with pressure and substrate temperature [23]. As illustrated in Figure 1-7, the high energy particles emitted from the hot surface generates a net force to lift the structure. This type of assembly can only be done in a vacuum environment, and the substrate need be heated. However, this method can be used for any surface micromachined system. Ultrasonic vibration energy is combined with thermokinetic force to reduce the static friction and make the thermokinetic force comparatively significant.
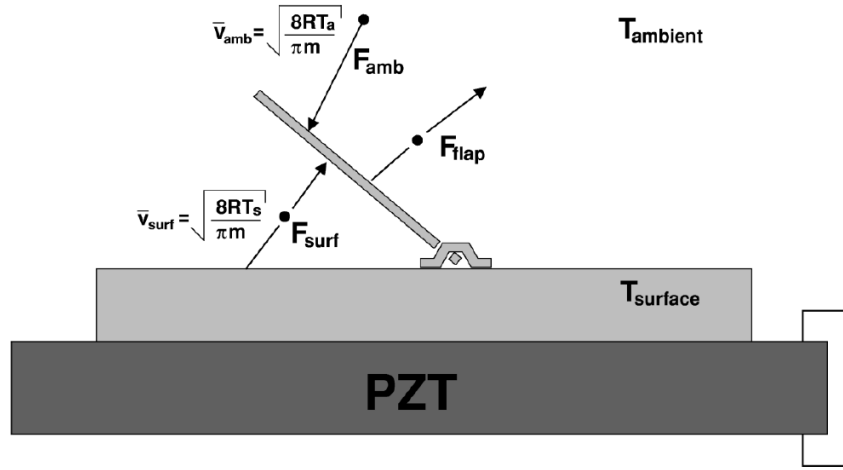
Figure 1-7: The origin of thermokinetic force [23]

Electrostatic batch assembly is another force driven assembly technique to assemble multiple micro-structures on a surface simultaneously. The system in [24] utilizes ultrasonic vibration equipment to generate friction between the polysilicon structures and the substrate. As described in Figure 1-8a, the friction makes the surface machined structures to charge and be lifted due to the repelling of like charges. Due to the "memory effect", the assembly occurs without further ultrasound actuation after the initial assembly. The apparatus sketched in Figure 1-8b is used in another electrostatic system in [25]. The ITO-coated glass slide is used as a global top electrode and connects with a DC power. Electrostatic force is generated between the glass slide and substrate to pull the structures away from the surface. PZT plate is driven by an AC source – the ultrasonic vibration here is used to facilitate the assembly by reducing stiction between the flip-up plates and substrate. These two parallel assembly techniques can reach nearly perfect yield over the entire die area. However, the structures can only be stabilized at the vertical position.
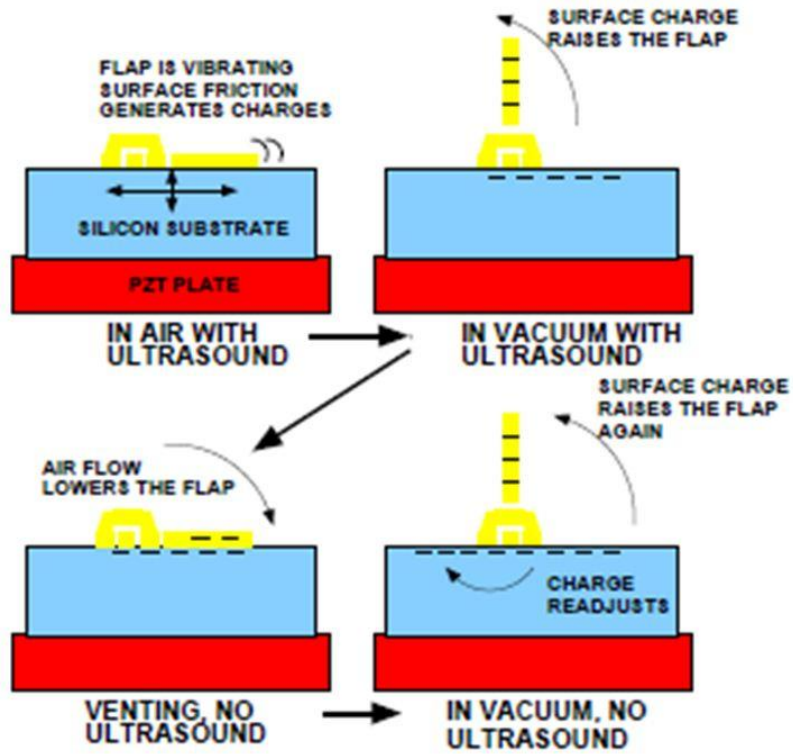
(a)
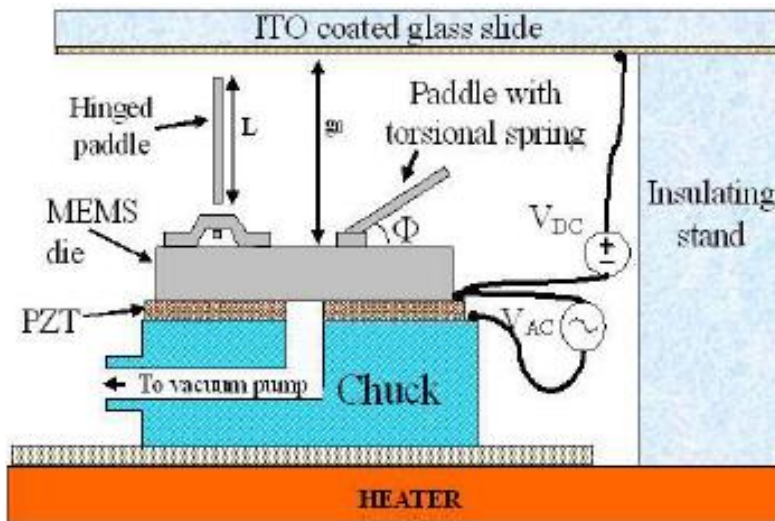
(b)

Figure 1-8: Electrostatic Batch Assembly (a) [24] (b) [25]

The liquid-based mechanisms are popular in recent years. As proposed in [26], the particles of the suspended liquid polymer or low melting point alloy collide with each other in a liquid medium. The resultant capillary force binds the particles together and makes the polymers

crossed-linked and the alloys solidified, as shown in Figure 1-9. Then a three-dimensional solidified structure is obtained. This method is also called capillary-force-based self-assembly. How to locate the particles at the desired locations is the main issue of this type of techniques.
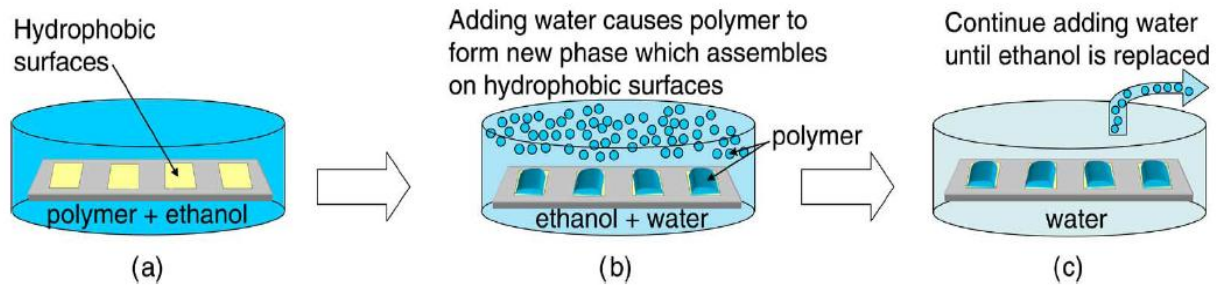
Figure 1-9: Schematic of the polymer deposition [26]

Chemical-based assembly [27] works in a similar way with the liquid-based techniques. It uses hydrophobic and hydrophilic materials for assembly. Basing on the desired three-dimensional shape, these materials are solidified by the bonding force between molecular as illustrated in Figure 1-10.
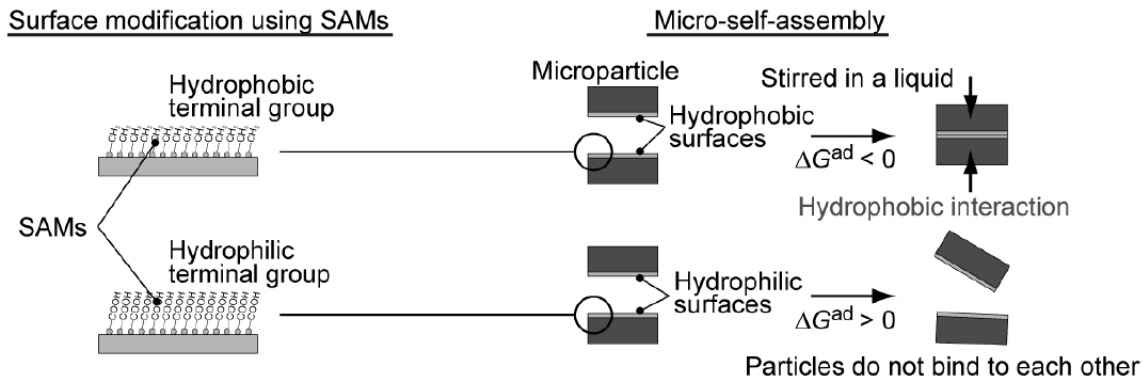
Figure 1-10: Bindings of microparticles [27]

Template-based assembly [28] is a wafer-level packaging strategy based uniquely orienting self-assembly. The parts to be assembled are initially spread in a single layer with the same face-orientation. Then the parts are aligned and anchored one-to-one to the template. Finally the parts are bonded to the substrate with the same in-plane orientation. These steps were demonstrated in

Figure 1-11 with two self-organizing parallel assembly processes: a semidry uniquely orienting process and a dry uniquely orienting process.
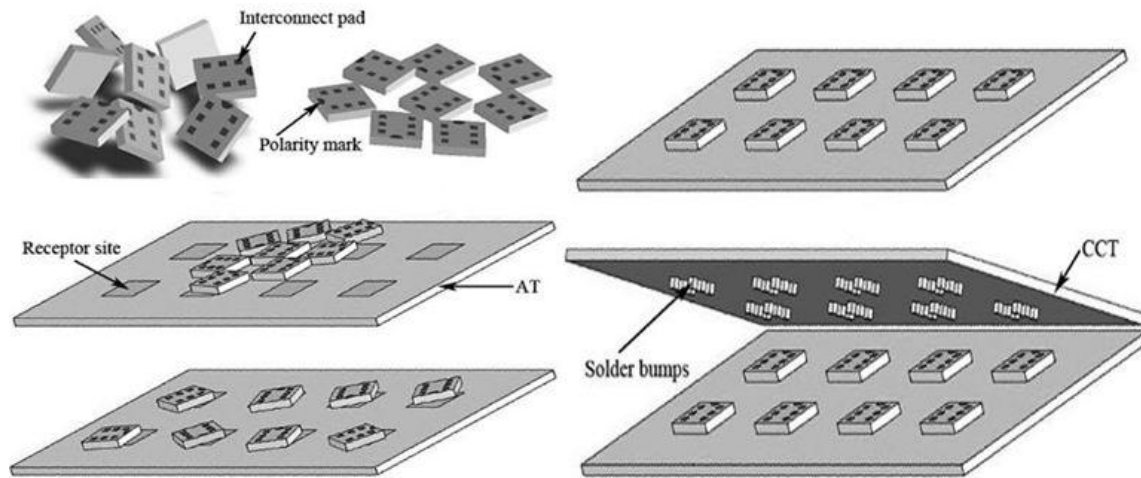
Figure 1-11: Template-based assembly process [28]

Thermal actuator [29] [30] [31] is composed of a hot beam and a cold beam as shown in Figure 1-12. Current is driven through the arms and results in the generation of thermal energy. Since the hot arm has a higher resistance, it generates more thermal energy and expands more than the cold arm. Then the actuator bends toward the direction of the hot arm.
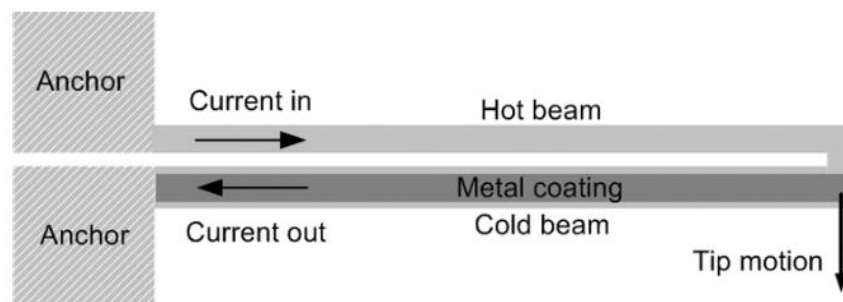
Figure 1-12: Schematic of the thermal actuator [29]

An auto-assembly system in [29] is driven by vertical thermal actuators and arrays of lateral thermal actuators. As schemed in Figure 1-13, the vertical actuator lifts the left free end of the flip-up plate off the substrate and makes the plate in an angle with the substrate. The lateral thermal actuators drive the lift arm to flip up the micromirror around its substrate hinges. When the mirror is lifted to the desired angle, it is held by a locking mechanism. Although the

displacement provided by thermal actuators is small, the generated force is large and the assembly is highly accurate.
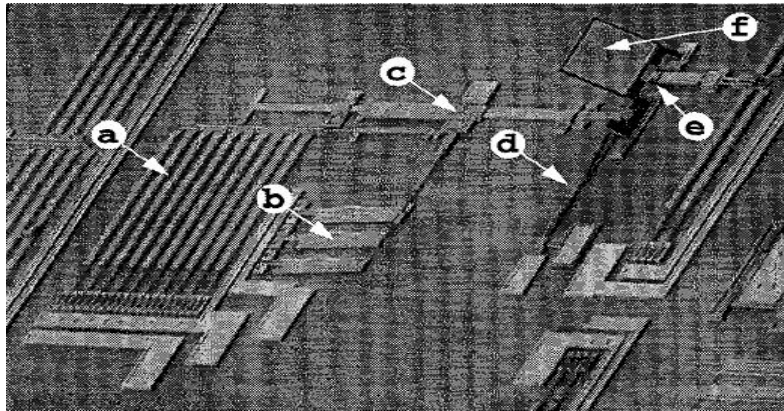
Figure 1-13: A thermal actuators based automated assembly system. The system consists of: a linear assembly motor (a drive actuator array (a), a coupling actuator array (b), and a drive arm (c)); a vertical actuator (d); an auto-engaging locking mechanism (e); and a scanning micromirror (f) [29]

(a)

(b)
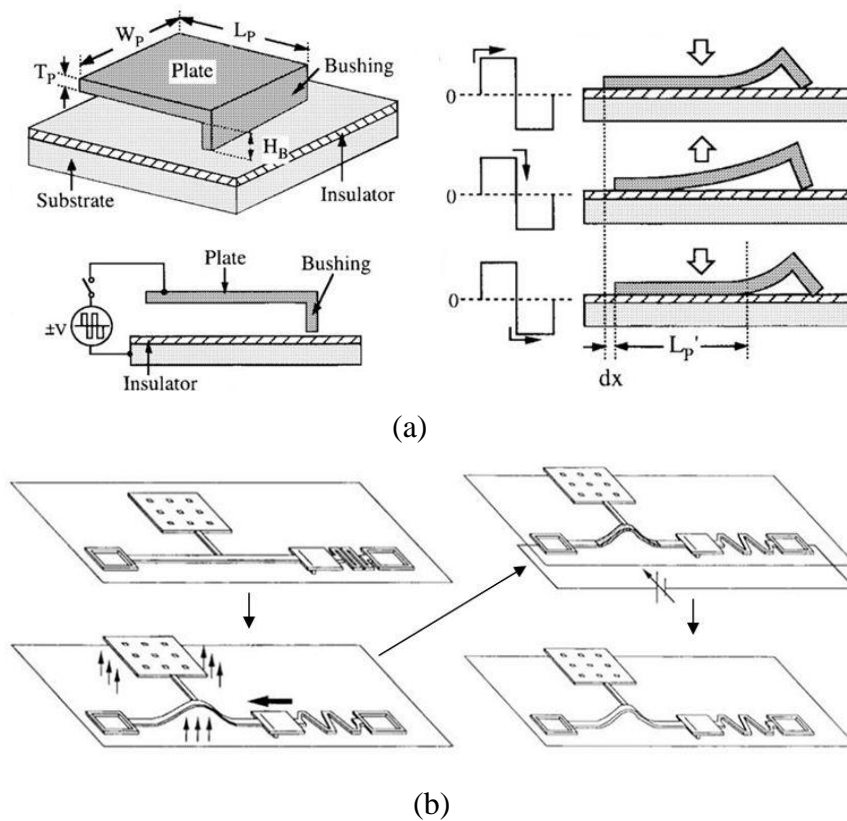
Figure 1-14: Scratch drive actuator (a) Working process of scratch drive actuator; (b) Scratch drive actuator based self-assembly structure [32]

13

The scratch drive actuator is a plate with a bushing on one end and locating on an insulator layer, which is on top of the substrate. When a voltage is applied, a capacitor is formed by the plate and the insulator layer, and then a periodical electrostatic force can be generated. As a result of the periodical electrostatic force, the scratch drive actuator moves forward in a step motion as the process depicted in Figure 1-14a. The plate is attracted to the substrate and deformed at the rise of the applied pulse. It then restores at the downward of the pulse under the restored elastic stain energy, while the bushing keeps contacting with the substrate, so the tail of the plate moves forward a small distance. When the plate is attracted down again, its tail is attracted to the substrate first, so the bushing tip moves forward in the deformation process of plate. These steps repeat under the continuous variant pulse and the plate moves forward in the step motion.

Scratch drive actuator is used in [32] to assemble a surface machined stage to form 3D structure. As illustrated in Figure 1-14b, one side of the scratch drive actuator is connected to the stage through an elastic beam and the tail end connects to a buckling beam. When the actuator is activated, the stage is lifted up from the substrate. While the scratch drive actuator pushes the stage out of plane, heat is generated by the current in the system and an annealing effect is caused. As a result, a plastic deformation is formed and the stage is held at that position permanently.

1.3.2 Applications of assembled structure

Functional MEMS devices, such as micromirrors, are usually built in the structures and used in various applications. Micromirrors, as one of the most popular optical MEMS devices, have applications generally in the following categories: telecommunications, projection display, 3D tracking and position measurement, laser marking, 3D scanning, etc. They usually have the advantages of compact size, high speed, low-power, and low-cost.

1.3.2.1 Optical switch

Under the stimulation of the huge market and profit of optical communication, MEMS based optical network technology has become a fast growing field. Optical switches are one of the most common MEMS applications in optical communication industry. Optical switch redirects input

light signal from one optical fiber to another. Optical switches can be separated to several types: conventional 1x2, 2x2 or 1xN switches, small NxN 2D switches (N < 32) and large NxN 3D switches.

   A simplest 2x2 digital switch is shown in Figure 1-15. A micromirror is located at the intersection of the light paths between input and output fibers. It does not interfere with the laser beams at the original position. When actuated by electronic signals, the micromirror pops up[33] or sticks out [34][35] to bisect the light beam during actuation, then light is directed or switched to the fiber in perpendicular direction.
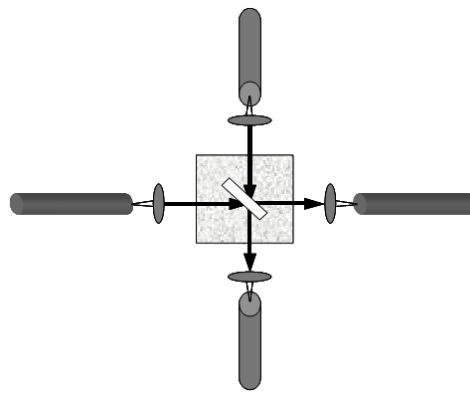
Figure 1-15: Simple 2x2 MEMS Optical Switch [37]

   These planar or 2D type conventional switches can be extended up to NxN switches and control light exchange among N laser beams. An example 8x8 switch is shown in Figure 1-16. Similar with the conventional 2x2 switch, each mirror rotates around a single axis and has only two positions. They are placed at the intersections of any two light paths between input and output ports. They can be in either the ON position to reflect light or the OFF position to let light pass uninterrupted. For the NxN type switches, a total of N^2 mirrors are required. The number of switches are usually limited to N=32 and below [36], since manufacturing yield, optical packaging of fibers and low loss performance become problematic at these switch sizes.

   For larger optical switches, 3D type switches are designed [38][39]. The configuration shown in Figure 1-17a includes two arrays of rotating mirrors. Each of the movable micromirrors can rotate about two-axis in an analog manner, as the detailed photograph in Figure 1-17b, instead of ON/OFF states. Any input optical beam can be directed to any output fiber through the reflection of two mirrors. In this kind of configuration, only 2N mirrors are required. Another 3D switch

shown in Figure 1-18 has a fixed mirror and one array of movable mirrors. The input optical beam is firstly reflected by a movable mirror to the fixed one, and then reflected back to another movable mirror which directs the beam out. In these systems, each mirror requires precision analog control. Furthermore, some method of feedback may be required to ensure the accuracy of pointing.
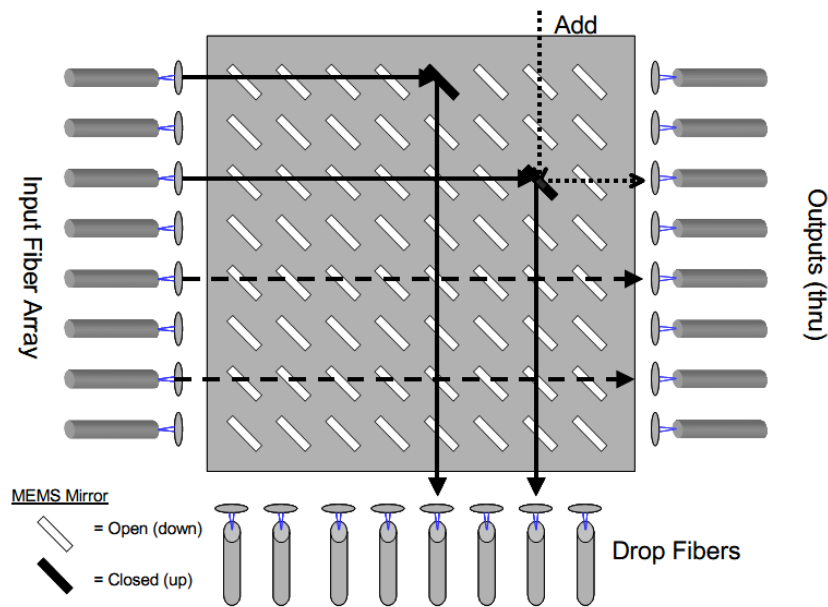
Figure 1-16: NxN, non-blocking optical switch [37]
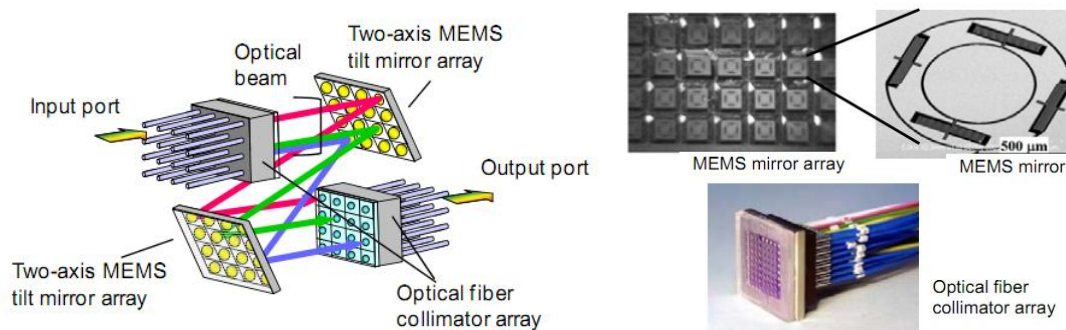
Figure 1-17: 3D MEMS optical switch and some switch components (a) Configuration of a 3D MEMS optical switch, (b) switch components [38]
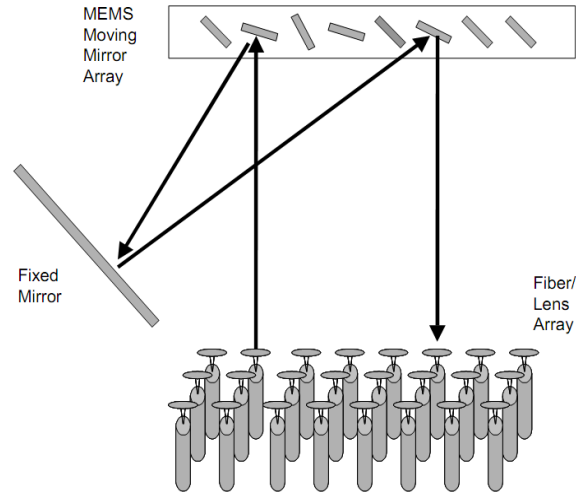
Figure 1-18: Large NxN switch using 3D beam steering [37]

1.3.2.2 VOA

Except for optical switching, MEMS technology is also widely used in optical communication transmission. VOA is used to solve the network equilibrium problem in DWDM (Dense Wavelength Division Multiplex) optical communication. It is able to transmit one or more laser beams at different wavelength in one optic fiber. With the development of optical communication network, the market demand for VOA is growing.

Two types of micromirror-based VOA are shown in Figure 1-19. The quantity of reflected laser beam and attenuation of signal is changed by moving with mirror. The flat packaging in Figure 1-19a occupies a relatively large area to hold the fibers on the substrate. In the system in Figure 1-19b, the input laser beam goes through optics lenses and reaches a micromirror, which tilts according the voltage of VOA input. The input laser beam from the first fiber is completed directed to the second fiber when the mirror is in horizontal position; otherwise, only part of the beam is directed to the second fiber.

VOA has the advantages of small size and low power consumption. Reliability is one of the key issues in VOA design. It need reach sufficient rotation angle and have sufficient strength to combat shock. The resonant frequency of the torsional mirror is designed to be higher than the noise in everyday environment in order to avoid the damage caused by resonance vibration.

17
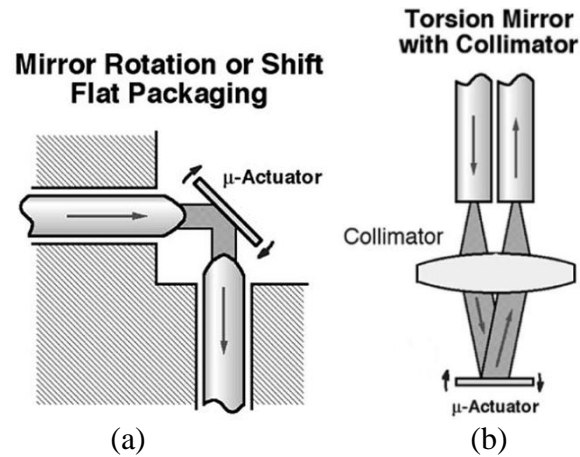
Figure 1-19: Micrmirror-based MEMS VOA (a) Flat packaging. (b) Coupling through a collimator lens [40]

1.3.2.3 DMD technology

Digital Light (DLP) technology from Texas Instruments is one of the MEMS based projection display techniques and Digital Mirror Devices (DMD) is the basic of this technology [41]. A DMD is an array of micromirrors and each micromirror is designed to tilt into (ON) or away from (OFF) a light source. The mirror tilts when a digital signal energizes an electrode beneath the mirror. The applied voltage causes the mirror corner to be attracted to the actuator pad resulting in the tilt of mirror. When the digital signal is removed, the mirror returns to original position. When a mirror is in the ON position, it reflects light towards the output lens; in the OFF position, the light is reflected away from the lens but to a light absorber (as shown in Figure 1-20a). This fast speed allows the production of projector composing of only one DMD light modulator, as illustrated in Figure 1-20b. Under the illuminating of white light, the RGB color wheel spins and sends red, green, and blue light to the DMD sequentially. At the same time RGB video signal is being sent to the DMD mirror-pixels. The mirrors are turned on depending on how much of each color is needed. The sequential images are integrated in the eye and a full color image is seen. High resolution images projected by DMD make it applicable in high definition electrical appliances, e.g. HDTV. However, since each reflective element represents one pixel on the display, it requires successful fabrication of M×N elements for a display with m rows and n columns.

(a)   (b)
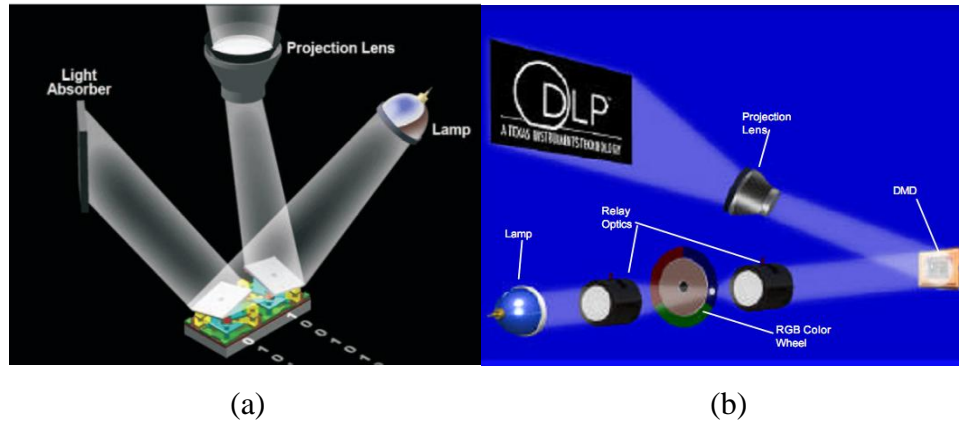
Figure 1-20: DLP projection system (a) Two mirror-pixels in On and Off State; (b) A one-chip DLP projection system [41]

1.3.2.4 Barcode reader

Barcode reader is a typical application built basing on the function of resonant scanning micromirror, as the diagram shown in Figure 1-21a. A laser beam focuses on the mirror through a focusing lens. The reflected beam projects to the image plane where the barcode is located. The entire width of the barcode is covered by the scan extent of micromirror. The backscattered light from the barcode is collected by a fast lens with large numerical aperture (NA) and detected by a silicon photodetector (Figure 1-21b). The light is modulated in accordance with the light and dark values of the bar-code symbol. The detected signal is then normalized and decoded.
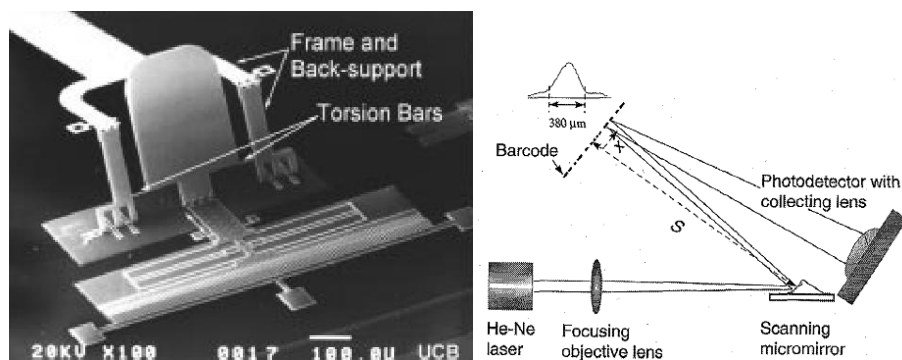
Figure 1-21: Resonant scanner and Barcode reader (a) SEM photograph of the resonant scanner and (b) Schematic of the barcode reader [42]

1.3.2.5 Projection display techniques

MEMS based projection display techniques have the advantages of high resolution, compact, and long life. They have been used in mobile communications, digital cinemas, data and video projectors, HDTVs, and other portable computing and personal electronics. Operating at the resonant frequency is an effective way for these display devices to reduce the power requirements.

A tilting micro-mirror that has a triangular waveform resonance response and a resonance frequency [43] is an example of this kind of devices. Raster scanning is done using tilting micromirror device, as shown in Figure 1-22. Raster scanning is a display method that scans the entire view by directing a light beam on the rectangular target screen. The view is divided into several scan lines and each scan line is subdivided into pixels. The number of scan lines multiplying with pixels is the resolution of the projected view. Bidirectional scanning is carried here, which means displaying a new line of data in both scan directions. Bidirectional scanning doubles the display rate of unidirectional scanning, who write data only during the forward direction, by permitting writing two lines during one scan cycle.
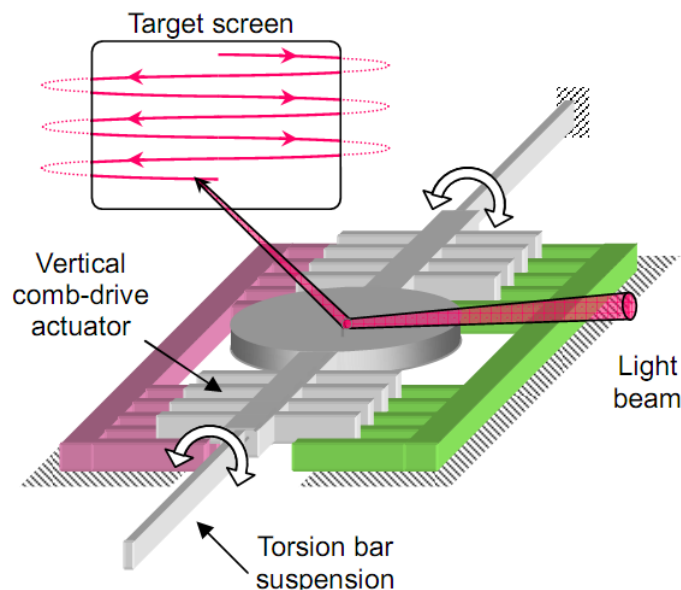
Figure 1-22: A tilting micromirror for horizontal scanning [43]

1.3.2.6 Tracking and positioning

Micromirrors have enabled the tracking and position measurement in a variety of situations with very low cost. They can be used in robotics, gaming and human-computer interaction applications. Milanović and Lo proposed a fast and high-precision 3D tracking and position measurement mechanism for object inside a conic volume in [44]. As it shows in Figure 1-23, two laser beams scan the same object through the reflection of two micro-mirrors, which are spaced by a known distance. Lasers search for the target through two micromirrors from the origin to the maximum scan angles until the target is detected. The origin is then updated with current position of the target and becomes the start point of next tracking. A quadrant photo-detector gives the (X, Y) positions of the center of target. A beam-motion dither measures its tilt-orientation. Therefore, the detector detects any rotational position. When the object is located by both systems, its position on Z axis is determined by the difference of X readings and actual space between two mirrors.
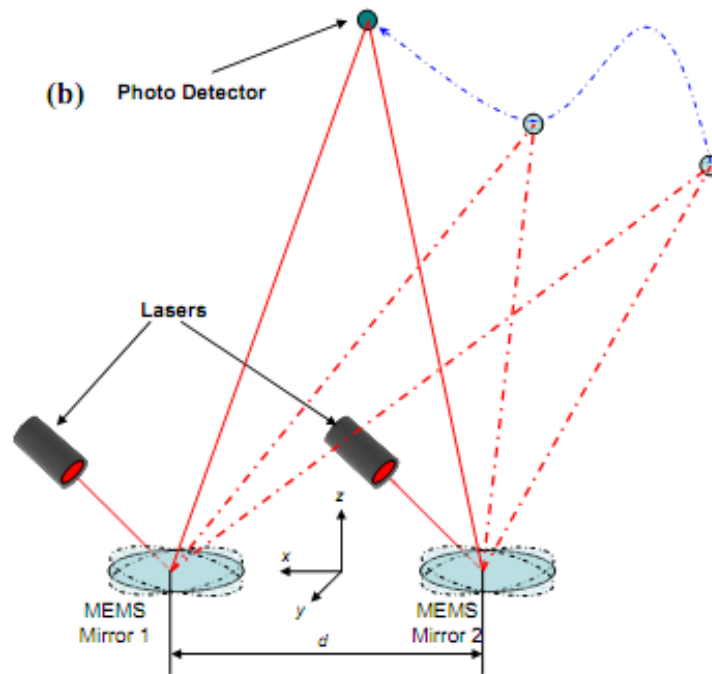
Figure 1-23: Schematic of a 3D tracking setup - two beam-steering mirrors aiming their laser sources onto the target [44]

1.4 Objectives

Among the various assembly techniques discussed above, limitations exist in some of them. For example, centrifugal force, magnetic force, thermokinetic force and electrostatic force based assembly techniques all require extra equipments. Also, damage can be caused to the micro structures when the substrate is heated during the thermokinetic force based assembly process. Magnetic force assembly is only applicable to magnetic materials, so that the production cost is increased by adding magnetic material to the micro structures. On the other hand, both centrifugal force and electrostatic force can only do batch assembly on structures with the same design. Since the same magnitude of force is applied on the entire wafer, some subtle parts on the structure are possibly damaged under this force. Furthermore, residual stress assembly is hard to control, so that complex operation is not possible. Liquid, chemical and template assemblies are not able to form complex 3D structures. Only thermal actuator and scratch drive actuator are able to assemble multiple devices of either the same or different designs on a wafer simultaneously without the requirement of any external equipment.

The objectives of this thesis are:
1) Develop a novel automated microassembly mechanism, which satisfies the following requirements:
    a. Capable of assembling without external interference,
    b. Suitable for wafer-level multi-devices batch assembly,
    c. Applicable to matured and commercial surface micromachining process, such as PolyMUMPs [45]
2) Design and modeling methods will be developed for the novel micro assembly mechanism.
3) Prototypes will be fabricated and tested to experimentally verify the novel micro assembly mechanism.
4) Applications of the micro assembly mechanism to MEMS devices will be studied

The report includes five chapters and is organized as following: Chapter 1 introduces the background information and overviews current automated assembly techniques; Chapter 2 presents the design of a novel automated assembly mechanism, including the introduction of its

components and working principle, graphical and analytical design methods, simulation of external forces withstood at the vertical position, and analysis of relations among each components; Chapter 3 describes the experiment processes and results; Chapter 4 introduces the designs of micromirror utilizing the proposed structure and its applications; followed by the conclusion in Chapter 5.

Chapter 2 System Design

2.1 PolyMUMPs

All the commercial fabrication processes have their specific rules that need be strictly followed to achieve successfully fabrication, so the fabrication process has to be firstly determined before the system design. Though MEMS devices can also be fabricated using customized micromachining processes, which provide more flexibility to satisfy users' different requirements on the design and materials, but the cost and risk are both high. To reduce the cost of fabrication, non-customized micromachining process is considered in this design.

Some popular commercial micromachining processes include Poly Multi-User MEMS Processes (PolyMUMPs) [45], Silicon-on-Insulator Multi-User MEMS Processes (SOIMUMPs) [45], Metal Multi-User MEMS Processes (MetalMUMPs) [45], Sandia Ultra-planar, Multi-level MEMS Technology 5 (SUMMiT VTM) [46], Micragem™[45], silicon germanium (SiGe) bipolar complementary metal-oxide semiconductor (BiCMOS) [48], etc.

The Multi-User MEMS Processes (MUMPs) is a commercial MEMS fabrication process. It provides the general users with cost-effective prototyping of MEMS products [49]. PolyMUMPs is one of the three standard processes provided by MEMSCAP Inc.

PolyMUMPs is a three-layer polysilicon surface micromachining process. It is developed on the base of the work done by Berkeley Sensors and Actuators Center (BSAC) at the University of California in the late 80's and early 90's. In order to support different designs, the thicknesses of the structural and sacrificial layers and the design rules are designed to suit most users [49]. As the cross sectional view shown in Figure 2-1, polysilicon is used as the structural material, deposited oxide (PSG) is used as the sacrificial layer, and silicon nitride is used as electrical isolation between the polysilicon and the substrate.

The wafer in PolyMUMPs is 150 mm n-type (100) silicon with 1-2 Ω-cm resistivity. To prevent the electricity from the electrostatic devices on the surface penetrating to the substrate, the surface of wafer is doped with phosphorus. A 600nm low-stress LPCVD (low pressure chemical vapour deposition) silicon nitride layer is deposited as an electrical isolation layer.

Poly0 is a 0.5μm LPCVD polysilicon film and the phosphosilicate glass (PSG) sacrificial layer Oxide1 deposited on it is 2.0μm thick. The first structural layer of polysilicon (Poly 1) is deposited with a thickness of 2.0μm. The second sacrificial PSG layer Oxide2 is 0.75μm thick. The second structural layer, Poly 2, is then deposited with 1.5μm thick. The final deposited 0.5μm metal layer is an optional layer that provides for probing, bonding, electrical routing and highly reflective mirror surfaces. Oxide1 and Oxide2 are removed at the end of the process to free Poly1 and Poly2 [49]. To facilitate the fabrication, some other levels, such as anchors, holes, dimple and via, are also defined in PolyMUMPs. Combining all the properties, functions and process of PolyMUMPs, it is suitable for the fabrication of an automated micro assembly mechanism. Therefore, the design is made basing on PolyMUMPs rules.

	Poly0		Poly1		Poly2		Metal
	Nitride		1st Oxide		2nd Oxide		
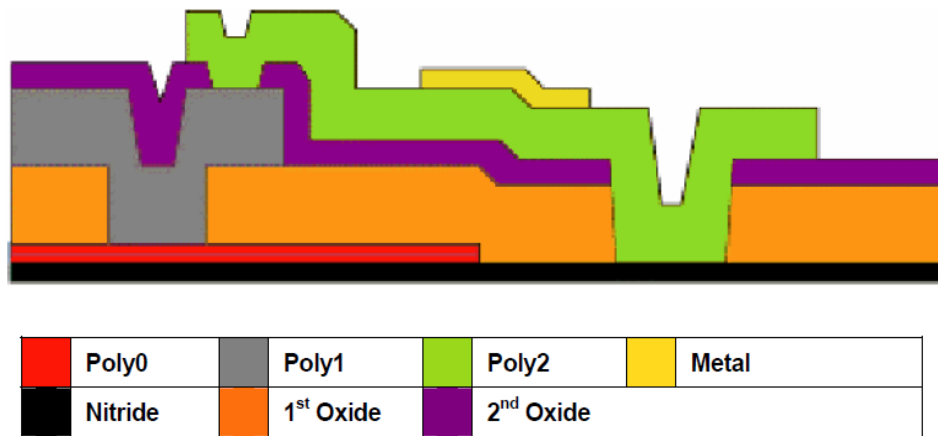
Figure 2-1: 7 layers of the PolyMUMPs process (cross sectional view) [49]

2.2 Repulsive force actuator

Because actuators based micro assembly mechanism suitable for wafer-level multi-devices batch assembly without external interference, they are chosen as the driven force of the automated assembly system. On the other hand, since the space is limited between the layers of PolyMUMPs process, repulsive force actuators which can overcome this limitation is adapted.

A repulsive force actuator [50][51][52] is consisted of unaligned fixed finger electrodes, aligned fixed finger electrodes and moving finger electrodes as shown in Figure 2-2 and Figure 2-3. When a voltage is applied, a potential difference is generated among these electrodes. The

moving finger electrodes are able to move away from the aligned fixed finger electrodes under a repulsive force. Since the electrodes move away instead of moving closer under the voltage, the repulsive actuator overcomes the limitation of pull-in phenomenon in attractive electrostatic actuators. Therefore, this kind of actuator can achieve a large stroke and eliminate the stiction phenomenon.
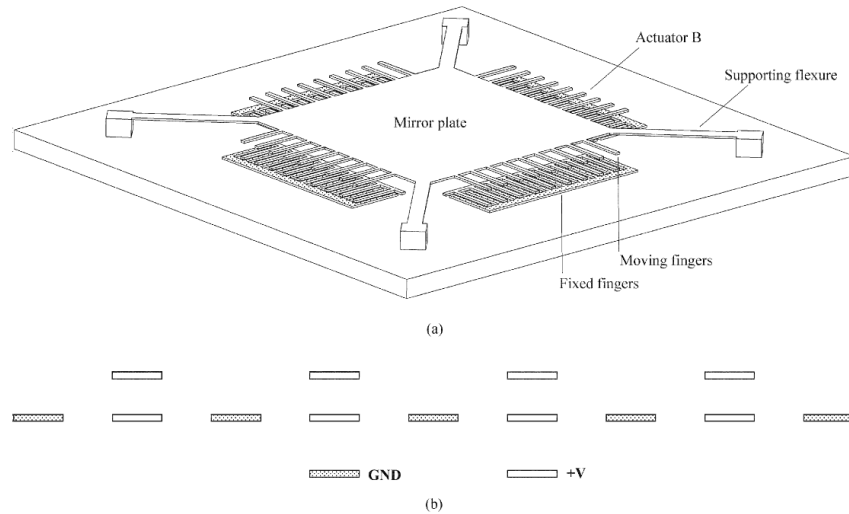
Figure 2-2: Basic form of repulsive force actuator: (a) translation micromirror driven by four actuators. (b) Section view of all the fingers in one actuator [51]
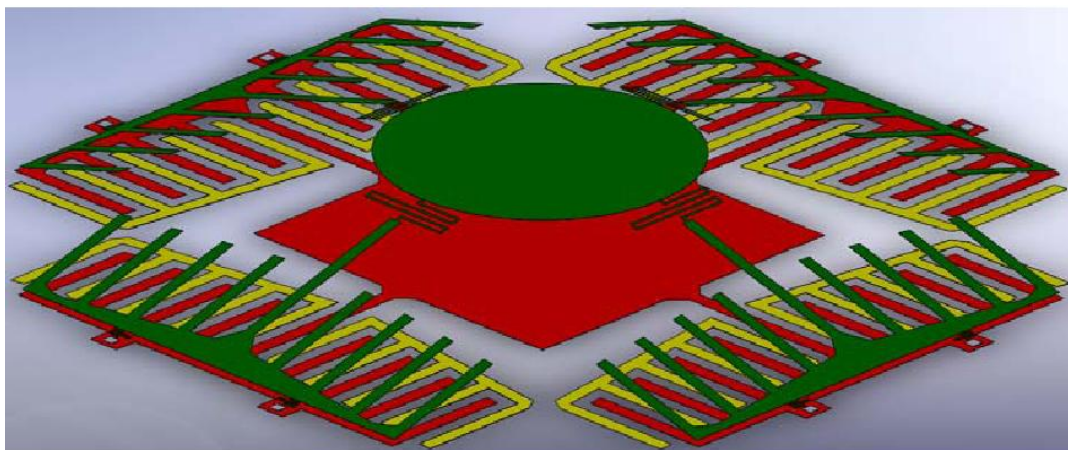
Figure 2-3: Large stroke out-of-plane translation micro electrostatic actuator [50]

2.3 System components and fabrication

The automated assembly mechanism proposed in this research consists of two rotational repulsive-force microactuators, hinges, two tethers and the flipping structure which is a functional MEMS device such as a micromirror for displaying, laser scanning or optical switching, or a tunable capacitor or a variable attenuator, etc., as shown in Figure 2-4. Each rotational repulsive-force actuator [50][51][52] is composed of fixed aligned and unaligned fingers, moving fingers and two suspension springs and a flipping beam (Figure 2-4a). The automated assembly mechanism is able to realize two types of assembling:

1) Assemble the flipping structure to a vertical position;

2) Assemble the flipping structure to an angled position with the angle ranging from $0°$~ $90°$.

Tether is a crucial part in the system to lock the flipped structure. A section of tether overlaps with the flipping structure, so tether is raised together with the flipping structure by the repulsive-force actuators when actuated. To ease the flip-up action of the actuators, spring is added to the tether because it is more yielding than a straight beam when bended. Between two types of springs - box spring (Figure 2-5a) and serpentine spring (Figure 2-5b), box spring is chosen. Comparing with serpentine spring, box spring is less elastic under the tensile stress because it has a small compliance value. It helps to achieve precise positioning. The box spring compliance C_b which is the reverse of spring constant and serpentine spring compliance C_s can be calculated using the Equations (2-1) (2-2) below [53]:

$$C_b = \frac{NL^3}{96EI} \tag{2-1}$$

$$C_s = \frac{L^3}{EI}\left(\frac{N}{12} + \frac{1}{48}\right) \tag{2-2}$$

Where E is Young's modulus, L is the length of the bars, N is the number of bars or boxes. I is the 2nd moment of inertia of the bars. For a rectangle, I equals to $bh^3/12$. Basing on the Equations, C_s is much larger than C_b, when L, N and I have the same values. Therefore, box springs do not extend as much as serpentine springs under tension. When the flipped structure is held by tether, it is less likely that spring extends under its weight.

27

Unaligned fingers (Poly0)
Aligned fingers (Pol0)
Moving fingers (Poly1)
Flipping beam (Poly1)
Tether (Poly2)
Hinge (Poly2 & Anchor2)
Suspension Spring (Poly1) & Anchor1

(a)

Upper Notch
Lower Notch

(b)

Flipping beam Left (Poly1)
Flipping beam Right (Poly1)
Tethers (Poly2)
Hinge (Poly2 & Anchor 2)

(c)
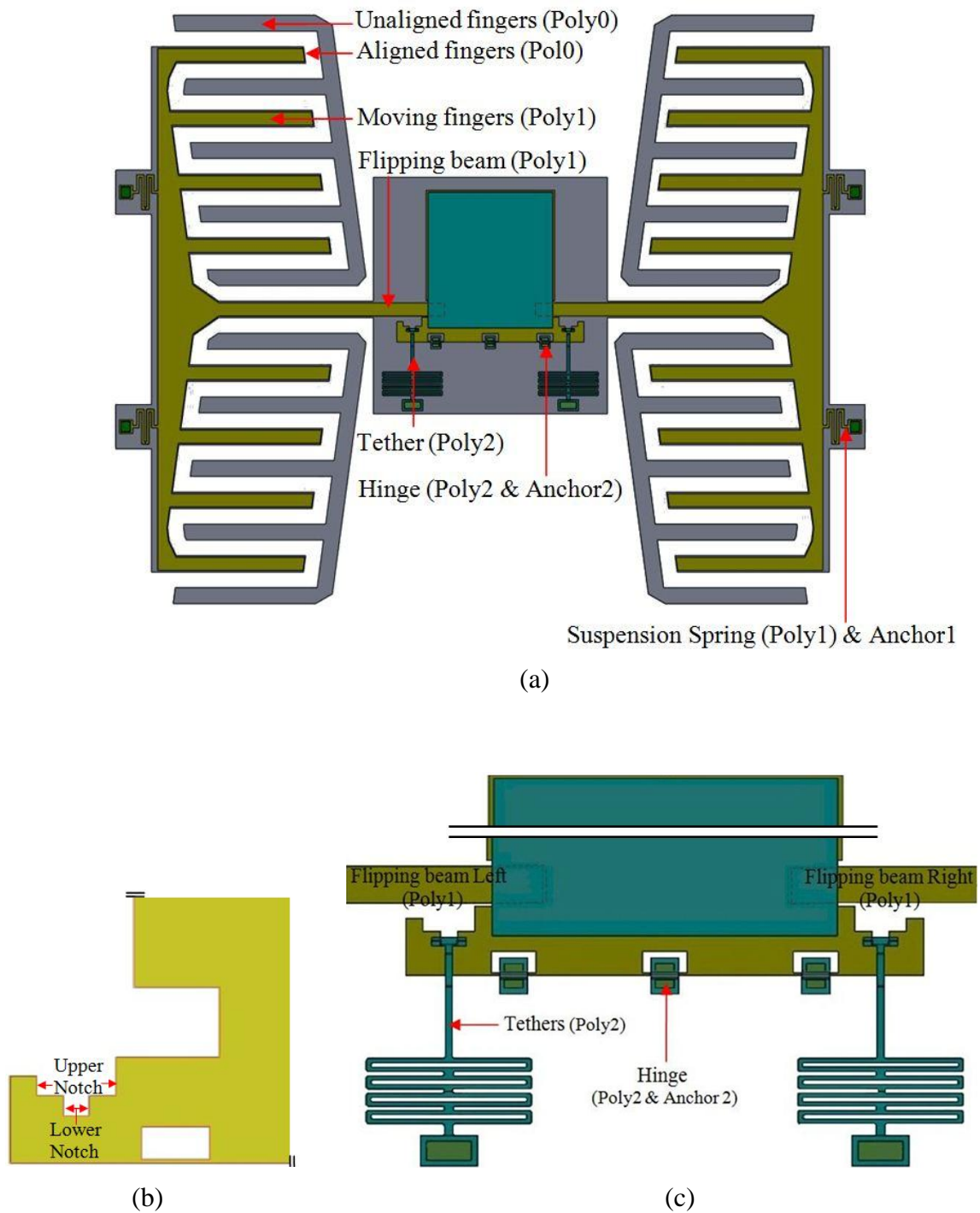
Figure 2-4: Repulsive-force actuator based automated assembly mechanism
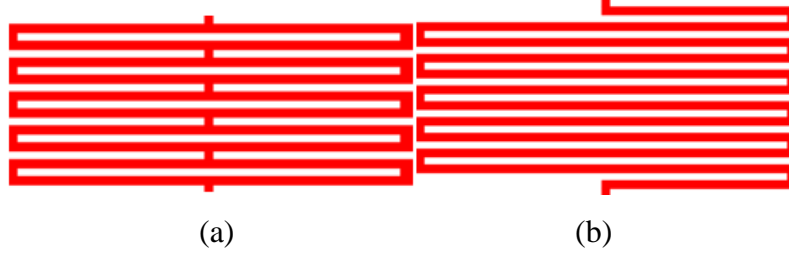
Figure 2-5: Spring (a) Box Spring; (b) Serpentine Spring [53]
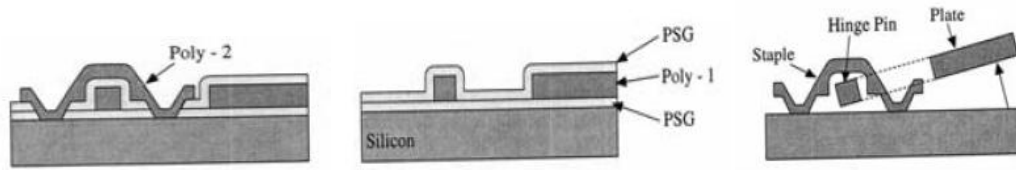
Figure 2-6: PolyMUMPs Process of Hinge Fabrication [54]

Hinge is another important component which enables the formation of three dimensional structures in surface micro-machining. Staple hinge is a common type of hinge. The type of hinge allows attached structures to rotate any degree within 180°. Because the rotating rod of a staple hinge is not circular in the practical fabrication, it need be checked if the rod can actually rotate inside the hinge. As the fabrication process shows in Figure 2-6, Equations (2-3) (2-4) (2-5) hold [53]:

$$d_h = w + 2t_{OXIDE2} \tag{2-3}$$

$$d_v = t_{OXIDE1} + t_{POLY1} + t_{OXIDE2} = 4.75\mu m \tag{2-4}$$

$$d = (w^2 + t_{POLY1}^2)^{1/2} \tag{2-5}$$

in which d_h, d_v and d represent the horizontal width, vertical height of hinge and diagonal of the rotating rod; w is the horizontal width of rotating rod; t_{OXIDE1}, t_{POLY1}, t_{OXIDE2} indicate the thicknesses of PolyMUMPs layer Oxide1, Poly1 and Oxide2, which are 2.0 μm, 2.0 μm and 0.75 μm, respectively. Therefore, the vertical height d_v is a fixed value 4. 75 μm. To have enough space to rotate the rod, the smaller one between d_h and d_v must be larger than the diagonal d.

To ensure the proper function of tethers, different designs of tether are modelled using Coventor®[55]. The forces applied on tether for each design are shown in Figure 2-7. For example, in order to lift the head of tether to 50μm, a force of 6.8μN need be applied on the tether which has no spring, but only 1.5μN force need be applied on the tether with 4-boxes spring. From the results, it can be seen that when the number of boxes increases, less force is required to lift the tether to a desired height.
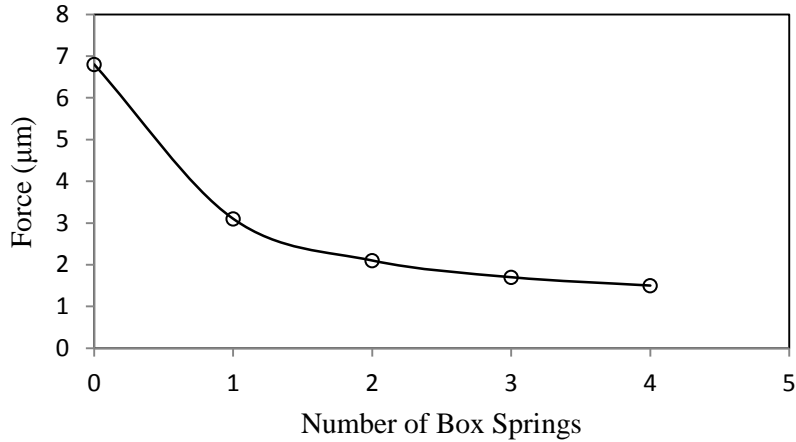
Figure 2-7: Applied force on different tether designs

The system is designed basing on PolyMUMPs [49] fabrication process. The flipping structure is a two layers structure - Poly1, Poly2 and connected by Poly1_Poly2_Via. Because flipping structure has a large surface area, this double layer design is to increase its rigidity and prevent it from bending when lifted up. Tethers are made on Poly2 and fixed by Anchor2 to Poly0 at one end. Hinges are made by the combination of Poly2 and Anchor2. Because of the large area of plate, holes and dimples (Figure 2-8) are fabricated on it.

2.4 Assembly to vertical position

2.4.1 Preliminary

When a voltage is applied to the two repulsive-force rotational actuators, the moving fingers along with the flipping beams rotates up and the flipping beams push the flipping structure up and away from the substrate. Even dimples are used, the stiction between the flipping structure and the substrate could still prevent the flipping structure from being pushed up. Hence, a

dynamic flipping is used to push the flipping structure up, i.e., a dynamic driving voltage (a square wave) is applied to the two repulsive-force actuators, such that the flipping beams apply an impact force to the flipping structure to break the stiction between the flipping structure and the substrate. After being released from the substrate, the flipped structure moves with an initial velocity provided by actuator and keeps rotating up about the hinges, due to the moment of inertial, until it is stopped by the steps on the tethers (see Figure 2-9c and Figure 2-9d) and held at the vertical position by the friction between the tether and the lower notch.

| (a) | (b) |
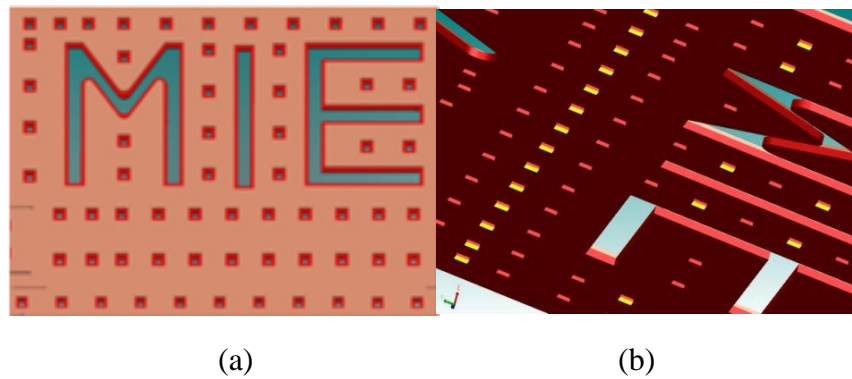
Figure 2-8: Holes and Dimples (a) Hole and (b) Dimple details

| (a) | (b) |

| (c) | (d) |
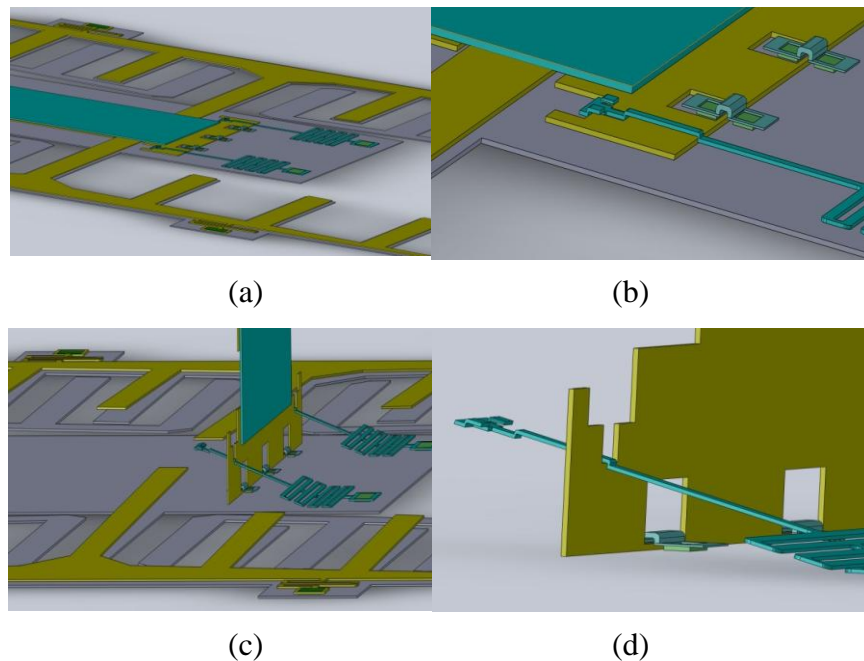
Figure 2-9: Structure before and after assembly (a) Structure before assembly; (b) enlarged view of structure before assembly; (c) Structure assembled at the vertical position; (d) enlarged view of structure assembled at the vertical position;

31

Since the section of the flipped structure, which interacts with the tethers, is fabricated using Poly1 and tethers are on Poly2, steps are formed on tethers due to the surface topography during the fabrication process by PolyMUMPs, as illustrated in Figure 2-10.
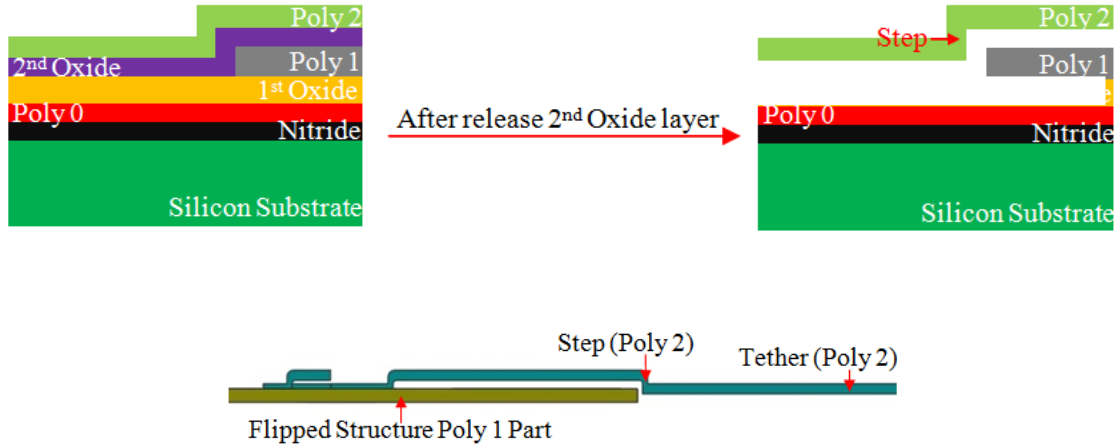
Figure 2-10: Steps on tether are formed due to the surface topography

2.4.2 Vertical angle

Vertical position assembly plays an important role in MEMS applications, such as controlling the throughput of optical beam in optical communication. To hold the flipped structure at vertical angle, two parameters are critical. One is the distance p_n from the bottom of the lower notch to the end of the structure, as indicated in Figure 2-11a and section AO in Figure 2-11b. The structure rotates around the edge that the end of the structure contacts with substrate, which is point O. Another parameter d is used to present the horizontal distance between the rotating axis of the structure and the rotating point O' on tether, which is assumed at the midpoint between the second and third box spring. Because of the release of oxide2 during the fabrication process, the distance between the end of the structure and the step is 0.75μm, which means the distance from the step to the rotating point on tether is d-0.75μm. The structure is considered as at the vertical position if the angle β it rotates is 90° or a little bit larger here. When β is larger than 90°, the structure is able to resist larger external forces.

To ensure the structure is stopped by steps at vertical position, one of p_n and d must be firstly decided and usually d is the first one decided, then other parameters can be calculated using

32

Equations (2-6) - (2-8). The values of p_n and d are usually limited by the available space on the substrate and the stiffness of tether. If the stiffness is too high, the structure cannot be flipped; if it is low, the tethers get bent easily.

In the triangle formed by the flipped structure in Figure 2-11b, the angle included by the structure and the tether is γ and the angle included by the tether and substrate is α. Angle γ and α can be derived using equation (2-6) and (2-8) basing on sine laws. Because of the thickness of the flipped structure, the base of the triangle in Fig 4a has a length of $(d-\frac{2}{\sin\beta}+2.75/\tan\beta)\mu m$ when β is more than 90°. The numeric value 2.75μm is the height difference of two rotating axis in the vertical direction, which is the sum of the thicknesses of Oxide1 and Oxide2 layers. And the hypotenuse of the triangle is $(d-0.75)\mu m$. So the other unknown parameter of p_n or d can be derived using equation (2-8). The three items in equation (2-8) represent the length of three sections of p_n: AB, BC and CO as indicated in Figure 2-11b.

(a)   (b)
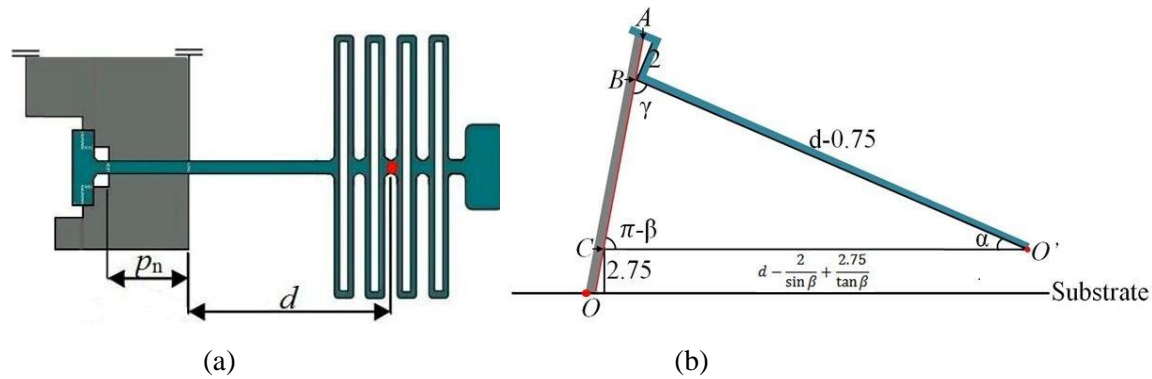
Figure 2-11: Top view and section view of flipped structure; (a) Top view of the flipped structure; (b) Flipped structure at the vertical position

$$\gamma = \sin^{-1}\frac{\left(d-\frac{2}{\sin\beta}+\frac{2.75}{\tan\beta}\right)\sin\beta}{d-0.75} \qquad (2\text{-}6)$$

$$\alpha = \pi - (\pi - \beta) - \gamma = \beta - \gamma \qquad (2\text{-}7)$$

$$p_n = \frac{2}{\sin\gamma} + \sqrt{(d-0.75)^2 + \left(d-\frac{2}{\sin\beta}+\frac{2.75}{\tan\beta}\right)^2 - 2(d-0.75)\left(d-\frac{2}{\sin\beta}+\frac{2.75}{\tan\beta}\right)\cos\alpha}$$

$$+\frac{2.75}{\sin\beta} \qquad (2\text{-}8)$$

33

2.4.3 Holding force
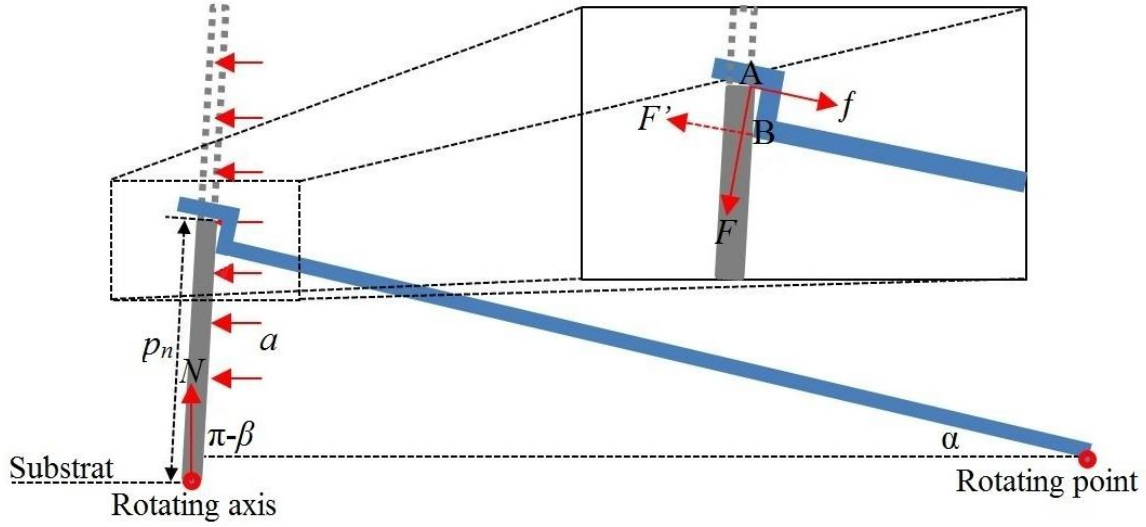
Figure 2-12: Forces at the vertical position

When the structure is flipped angle β to the vertical position, it is subjected to four forces: a restoring force F, a supporting force F', a friction force f, and a normal force N. The restoring force F is generated at the contact point A caused by the deformation of the box springs with the direction perpendicular to the lower interface of tethers (as shown in Figure 2-12). The supporting force F' exists at point B due to the resilient force from compressed tether, whose direction is perpendicular to the step on flipped structure. To prevent the flipped structure from dropping back, the static friction f exists along the contact interface and opposite to the motion trend of flipped structure. At the same time, the normal force N is exerted by the substrate and acted on the structure. The weight of the flipped structure is negligible here by comparing with other forces

Under an external force, torque $\tau_{F'}$ generated by supporting force F' decreases accordingly. Once the sum of torque $\tau_{F'}$ and the torque of external force τ_a overcomes the torque of static friction force τ_f, the flipped structure loses contact with the step and supporting force F' disappears, then the flipped structure drops back and is locked by tethers. In order to calculate the external force that the system can withstand, a uniformly distributed force is supposed, which can just overcome the friction. At this critical point, the value of maximum static friction force can be obtained using Equation (2-9), where μ is the static friction coefficient between

34

polysilicon, and the magnitude of N is calculated in Equation (2-10), where α is the angle tether rotates.

Because of the irregular shape of the flipped structure, it is divided into 16 parts and the torque generated by each of them is calculated using $a\rho t_i \int y_i \, dA_i$, where a is the acceleration caused by the external force, ρ is the density of polysilicon, t is the thickness, $\int y_i \, dA_i$ is the moment of area of each part, dA is the element area, y is perpendicular distance from the centroid of each element area to the rotating axis. Torques are also generated by the component of the restoring force F in the horizontal and vertical direction, which are τ_{Fx} and τ_{Fy}, respectively. And the torque generated by the friction f is expressed using τ_{fx} and τ_{fy}. If $\sum \tau$ in Equation (2-11) is positive, the structure will drop back. By counting two tethers in the system, torques generated by F, and f are multiplied by 2.

As the simulation shows in Coventor and Ansys, the force is $1.8\,\mu N$ when the step on tether is raised to a height of p_n, which means the flipped structure reaches the vertical position. Because the force used to lift the tether is equal to the magnitude of restoring force, F is obtained. In Equation (2-11), the value of p_n is 35.5μm in practical design, the actual flipped angle β is 95 °, angle α is deduced using cosine rule which is 15 °, f is derived from equation (2-9) using static friction coefficient 0.4 [56] between polysilicon interface, and N is from equation (2-10), so that acceleration α is calculated to be 7.6g.

$$f = \mu F \tag{2-9}$$

$$N = F\cos\alpha + f\sin\alpha \tag{2-10}$$

$$\sum \tau = \tau_a + 2\tau_{Fx} - 2\tau_{Fyfy} - 2\tau_{fx}$$
$$= \sum_{i=1}^{16} a\rho t_i \int y_i \, dA_i + 2F\sin\alpha\, p_n \sin(\pi - \beta) -$$
$$2(F\cos\alpha + f\sin\alpha)p_n\cos(\pi - \beta) - 2f\cos\alpha\, p_n \sin(\pi - \beta) \tag{2-11}$$

2.5 Assembly to angled position

2.5.1 Angled position

When an applied force is large enough to overcome the friction between the structure and the tethers, the flipped structure cannot be held at the vertical position and then falls back. A locking system in this mechanism, composed by tethers and notches (see Figure 2-4b) on the flipped plate, is used to lock the structure. The upper notch is wider than the width of the tether head, while the lower notch is narrower than it. Since the rods of tethers slide into the notches on the structure in the process of being flipped up, the heads of tethers are able to hold the structure when it falls to the designed angle within $0°\sim 90°$ as described in Figure 2-13.

(a)   (b)
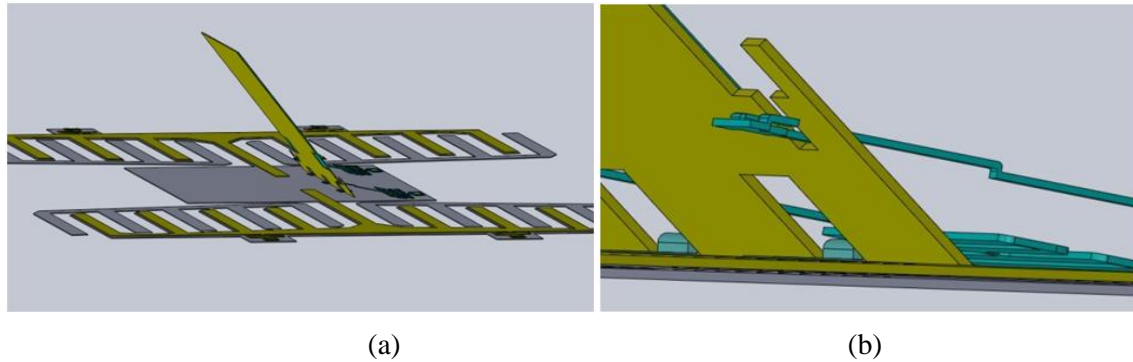
Figure 2-13: Structure assembled at the angled position

2.5.2 Design

In order to design a system with a desired flip-up angle β between $0°$ and $90°$ (as shown in Figure 2-14), two approaches are used including a graphic and a mathematical method.

In addition to p_n, d and α, more parameters of the system need be determined:

- p_w - the distance between the end of upper notch B and the end of the flipped structure;
- t_1- the length of tether between the rotating point O' and the point which contacts the end of lower notch A on the flipped structure;
- t_2 - the length of tether from the end of tether's head B to its rotating point.

Some related numeric values include the thicknesses of the flipped structure, tether and anchor which are 2μm, 1.5μm and 2.75μm, respectively. The height difference of two rotating axis is 2.75μm in the vertical direction that is the sum of thicknesses of Oxide1 and Oxide2 layers.

(a)

(b)
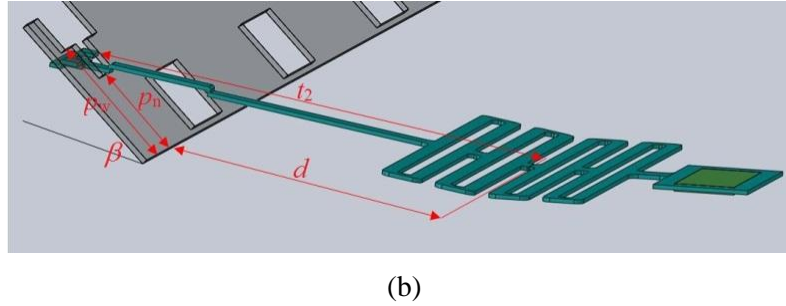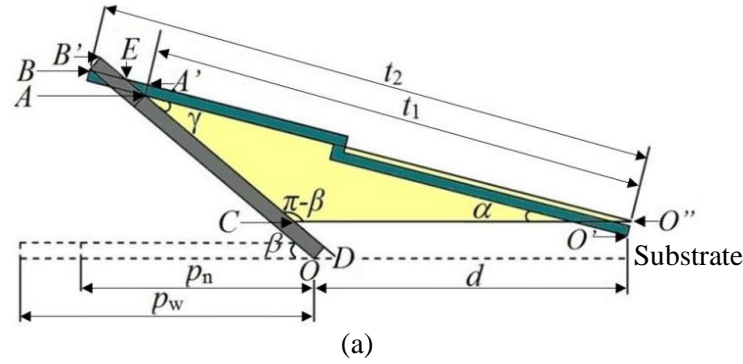
Figure 2-14: Parameters of the structure: (a) Sideview; (b) 3D view

2.5.2.1 Graphic method

Using the graphic method, parameters p_w and t_2 can be determined by several steps as illustrated in Figure 2-14.

1. Draw a rectangle with width p_n and height 2μm to represent the side view of the structure.
2. Rotate this rectangle angle β around its axis O in clockwise direction.
3. Find a point in distance d to the right side of the structure; then locate another point 2.75μm above it, which is the assumed rotating point of tether O'.
4. Draw a circle around O' with radius 2μm and a straight line from point A tangent to this circle at point O''. This line represents the lower face of the tether which section is over the flipped structure. As the existence of POLY1, the section of tether over the flipped

37

structure is 2μm higher than the other sections. Point A is the first contact point of the flipped structure and the tether, where the bottom of the lower notch touches the bottom surface of the tether. Its distance to the plate end is p_n and the distance to O'' is t_1.

5. Make another line parallel to the tangent line with distance 1.5μm. Since POLY2 has a thickness of 1.5μm, this line represents the upper surface of the tether.

6. Extend the rectangle until its bottom side intersects with the upper surface of the tether at point B. Point B is the second contact point of the flipped structure and the tether, at which point the bottom of the upper notch contacts with the end of tether head. The distance measured from B to O is p_w and the perpendicular distance from B to the extension line of $O'O''$ is t_2.

2.5.2.2 Analytical method

Besides the graphic method following the steps above, these parameters can also be determined by an analytical method. A trial-and-error method is used here. A temporary value of α is firstly assumed, e.g. 10˚, as of Equation (2-12). When p_n, d, *and* β are known, α_{temp} is substituted into Equations (2-13) - (2-16), so that t_1,γ, t_2 and p_w can be derived in turn, in which γ is opposite angle of edge CO'' in triangle $\Delta ACO''$. Using Equation (2-17), the actual value of α under this condition is obtained and then compared with α_{temp}. When the error is small, all the desired parameters are determined.

Equations (2-13) and (2-14) are deduced basing on cosine and sine theorem in triangle $\Delta ACO''$. And Equation (2-17) is derived basing on the relations of internal angles in this triangle. Line CO'' is drawn parallel to the substrate and intersects with the upper face of the flipped structure at point C. Lengths of AC and CO'' are expressed by the first and second bracket on the right side of Equation (2-13).The length of AC is the difference of AD and CD. Line AC is extended to intersect with the substrate at point D. The extended distance is $\frac{2}{\tan\beta}$, so length of AD is $p_n + \frac{2}{\tan\beta}$.The height of O'' to substrate $L_{O''S}$ is the sum of the distance from O' to substrate and the projection of segment $O'O''$ in the vertical direction, which is $2\cos\alpha_{temp}$, so the length of CD is $\frac{L_{O''S}}{\sin\beta}$. Edge CO'' is parallel to d but extended on both sides. On the left side, the extended length

equals to the horizontal projection of *CD* minus length *OD*, which is $\frac{L_{O''S}}{\tan\beta} - \frac{2}{\sin\beta}$. On the right side, the extra length is $2\sin\alpha_{temp}$. Then the length of *CO''* is written as the sum of these three sections.

$$\alpha_{temp} = \frac{10}{180}\pi \tag{2-12}$$

$$t_1^2 = \left(p_n + \frac{2}{\tan\beta} - \frac{2.75 + 2\cos\alpha_{temp}}{\sin\beta}\right)^2 + (d + \frac{2.75 + 2\cos\alpha_{temp}}{\tan\beta} - \frac{2}{\sin\beta} + 2\sin\alpha_{temp})^2$$

$$- 2\left(p_n + \frac{2}{\tan\beta} - \frac{2.75 + 2\cos\alpha_{temp}}{\sin\beta}\right)(d - \frac{2}{\sin\beta} + \frac{2.75 + 2\cos\alpha_{temp}}{\tan\beta} + 2\sin\alpha_{temp})\cos(\pi - \beta) \tag{2-13}$$

$$\frac{t_1}{\sin(\pi-\beta)} = \frac{d - \frac{2}{\sin\beta} + \frac{2.75 + 2\cos\alpha_{temp}}{\sin\beta} + 2\sin\alpha_{temp}}{\sin\gamma} \tag{2-14}$$

$$t_2 - t_1 = \frac{2}{\sin\gamma} + \frac{1.5}{\tan\gamma} \tag{2-15}$$

$$1.5^2 + (t_2 - t_1)^2 = 2^2 + (p_w - p_n)^2 \tag{2-16}$$

$$\alpha = \beta - \gamma \tag{2-17}$$

Equations (2-15) (2-16) are based on the intersection of the tether and the flipped structure. Segment *BA'* on the tether has length t_2-t_1 and is composed by two sections – *BE* and *EA'*. Since angle *AEA'=BEB'= γ,* Equation (2-15) is obtained. By connecting point *A* and *B*, this segment *AB* is a hypotenuse of two right triangles, *ΔABA'* and *ΔABB'*. Triangles *ΔABA'* is formed by the edge t_2-t_1 and the thickness of the tether. Triangles *ΔABB'* is formed by the edge p_w-p_n and the thickness of the flipped structure. Because they share the same hypotenuse *AB*, Equation (2-16) is derived.

The graphical and mathematical methods can be combined in the structure design. Or use one of them to design and the other one to verify the dimensions of each part.

2.5.2.3 Prototype design

A prototype with a flip-up angle $20°$ is designed using the approaches explained above. By considering the errors exist in the fabrication, the actual length of p_w is a little longer. This length

change increases the rotating angle of the tether, but does not affect the desired flip-up angle. The dimensions of each part are listed in Table 2-1~Table 2-3.

Table 2-1: Part Dimensions of Repulsive-Force Actuator Based Structure

	Plate (POLY1)	Plate (POLY2)	Plate (POLY_POLY2_VIA)	Upper Notch	Lower Notch	Dimple/ Hole 1	Hole2
Length (μm)	486.5	435	423	15	15	4	8
Width (μm)	412	400	388	60	20	4	8

Table 2-2: Part Dimensions of Tether

	Tether Head	Spring	Rod (Head End to Spring)	Rod (Spring End to Anchor)	Base (Tether)	Anchor2 (Tether)
Length (μm)	10	5 (bar) / 5 (gap)/75(total)	130	14	66	22
Width (μm)	40	191	8	8	35	52

Table 2-3: Part Dimensions of Hinge

	Hinge (Total)	Anchor2 (Hinge)	Rotating Rod
Length (μm)	32	10	2
Width (μm)	42	22	2

Chapter 3 Experiment results

Prototypes with a designed flip-up angle of 20 ± 1 °were fabricated by CMC Microsystems [57] using PolyMUMPs surface micromachining technique. Tests were carried out on these prototypes and completed in two stages. In the first stage, prototypes were assembled to the vertical position; in the second stage, the systems were then tested under external forces and the assembled angles were measured.

3.1 Vertical position

3.1.1 Assembly experiment setup

The experimental setup is illustrated in Figure 3-1. Prototypes were connected on printed circuit boards as shown in Figure 3-2a. PRAGMATIC 2416A 100MHz Waveform/Function Generator (Figure 3-2b) acted as the power generator to provide static and dynamic voltages to the prototypes. A 25x amplifier, TEGAM Model2350 High-Voltage Amplifier (Figure 3-2b), was used to amplify the applied voltage. Prototypes were observed and measured under a Zygo optical interferometer (Figure 3-1) and a SEM (Figure 3-3).
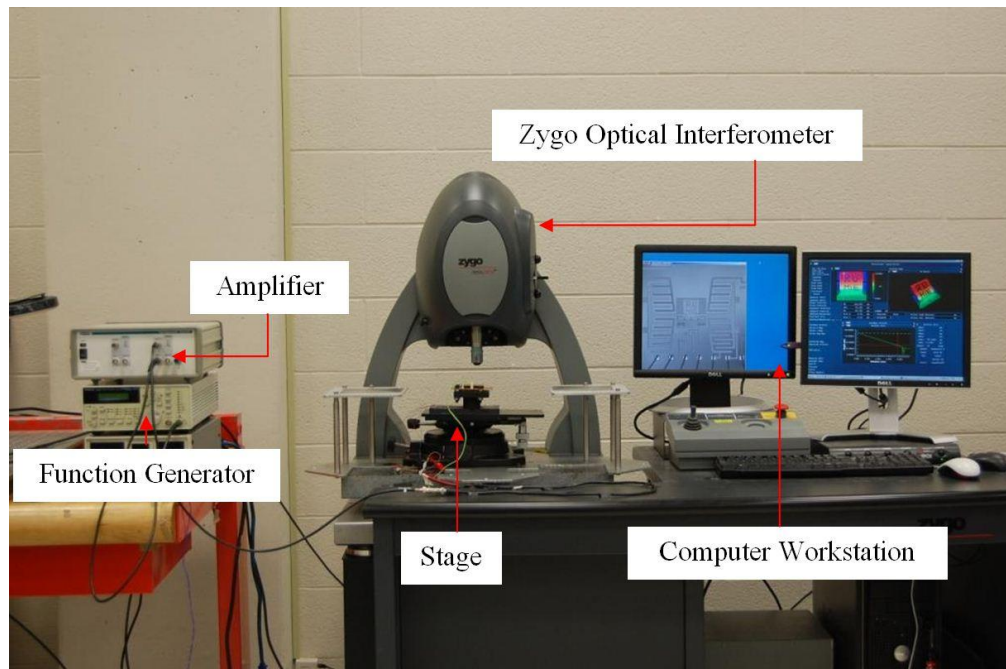
Figure 3-1: Assembly experiment setup and Zygo optical interferometer
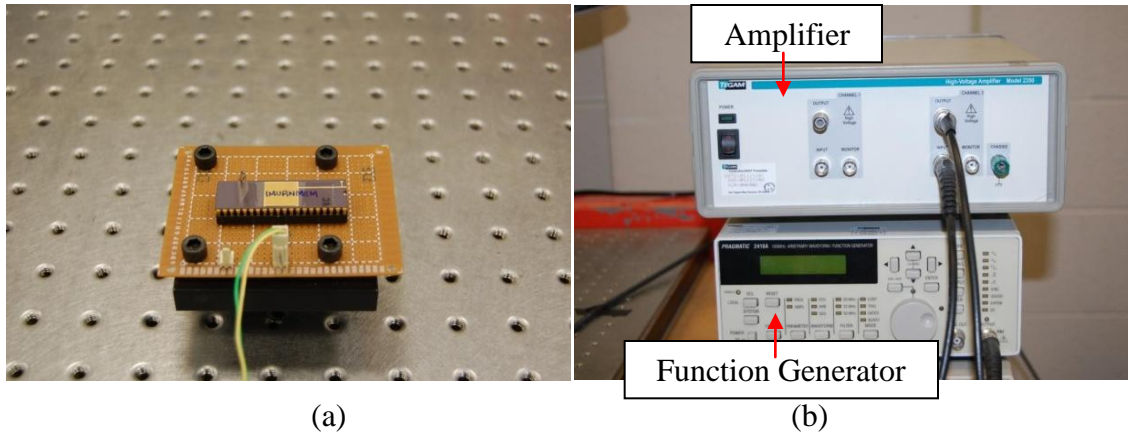
Figure 3-2: Equipment Setup (a) Connected prototype, (b) experiment equipments: TEGAM Model2350 High-Voltage Amplifier and PRAGMATIC 2416A 100MHz Waveform/Function Generator

Figure 3-3: SEM

3.1.2 Assembly process

In order to test the existence of stiction, a 200V step input was firstly applied on the prototypes during experiment. The movement of fingers on the repulsive-force actuators was observed but no response from the flipping structure.

To overcome the stiction, power was turned ON and OFF repeatedly on the first prototype. After several repentances, the flipped structure rotated to the vertical position suddenly and blocked by the steps on tethers (Figure 3-4c).
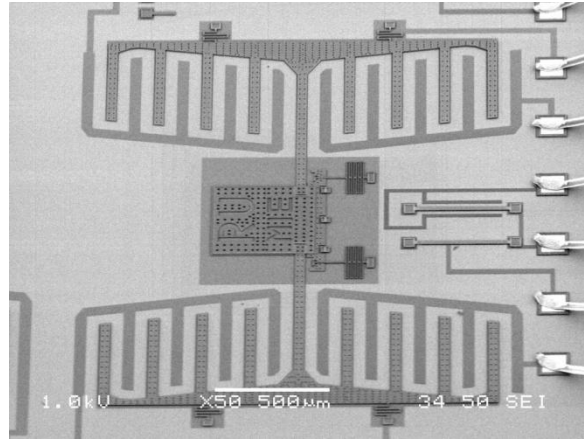
(a)
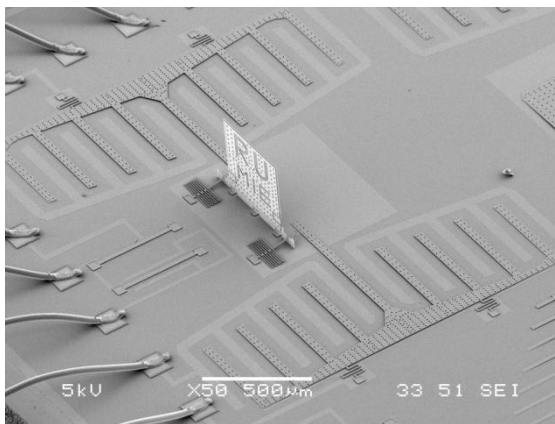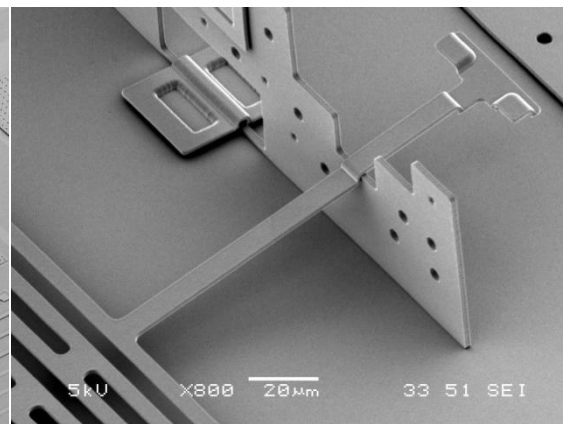
(b)   (c)
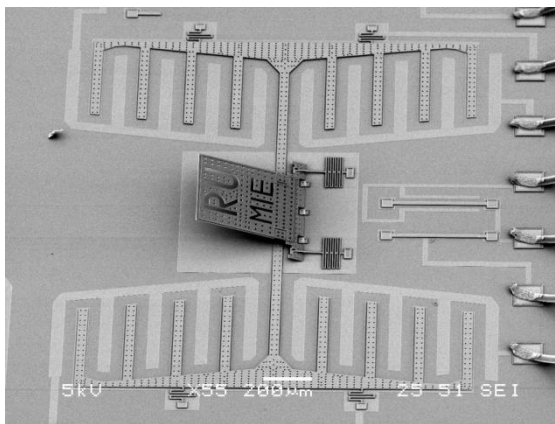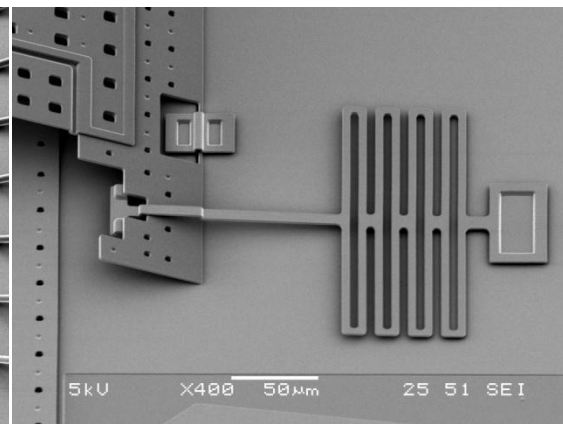
(d)   (e)

Figure 3-4. Pictures from SEM (a) Structure before assembly; (b)(c) Flipped structure is held at the vertical position; (d) (e) Flipped structure is blocked by tether at 20˚

On other two prototypes, dynamic driving voltage (square wave) was then applied after the initial 200V step input. Starting from 50V with frequency 1Hz, the voltage was kept on for 15 minutes and then increased with 25V increment, if the flipping structure was not flipped up. One of the prototypes was flipped at 150V and the other one was up at 175V. Similar with the first sample, the flipped structure were raised to the vertical position directly and kept at the position under friction.

All the tests showed the same phenomenon. When a small voltage was applied, the force exerted by the repulsive force actuators was not large enough to overcome the stiction effect. After several repeats of step inputs or the application of AC, the flipped structure was gradually loosed from the substrate, rotated to the vertical position and then held by tethers, as shown in Figure 3-5. As a simulation in Coventor showed, the maximum angle that the flipping beam formed with substrate was 3.18° and the maximum height it reached was 57.86μm. With a distance of 85.5μm between the flipping beam and the rotating axis of flipped structure, the angle that the structure can be lifted by the flipping beam is no more than 34° because their relative location. It proved that the flipped structure was not lifted to the vertical position by the flipping beams, but by inertia.
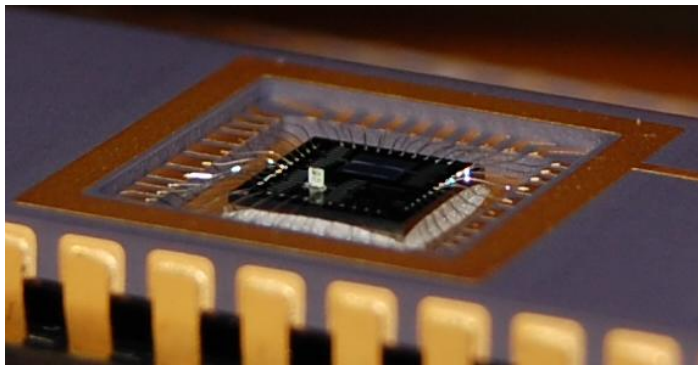
Figure 3-5: Prototype at the vertical position during test

3.2 Angled position

The flipped structure held at the vertical position will fall down when an external force is large enough to overcome the frictions between the flipped structure and tethers. In order to obtain the

magnitude of external force that the flipped structure can withstand without falling down, tests were carried out using the equipments as shown in Figure 3-6.
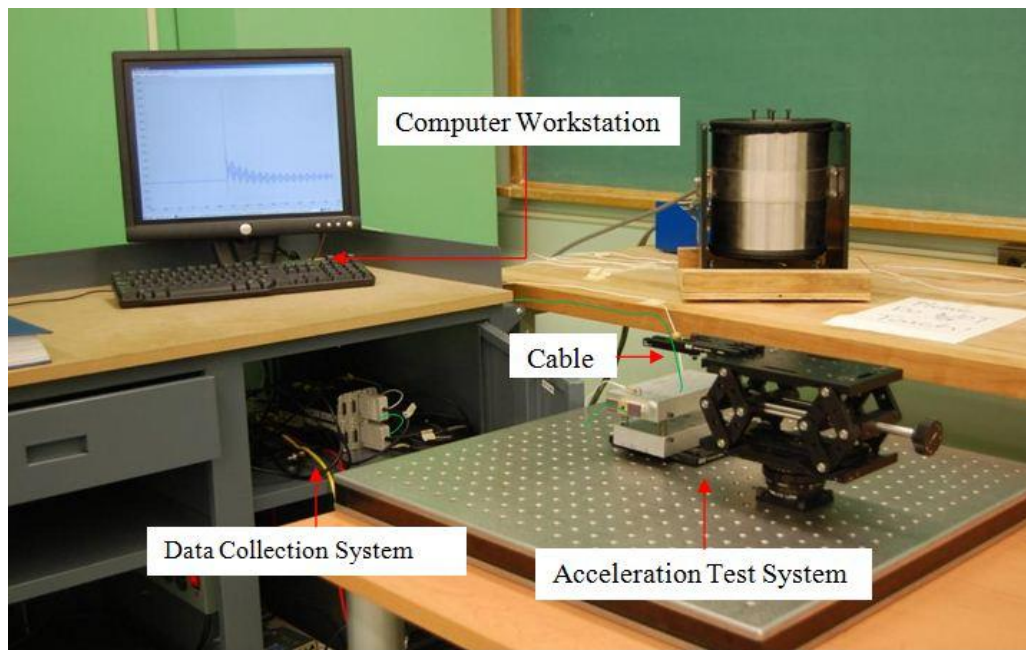
(a)
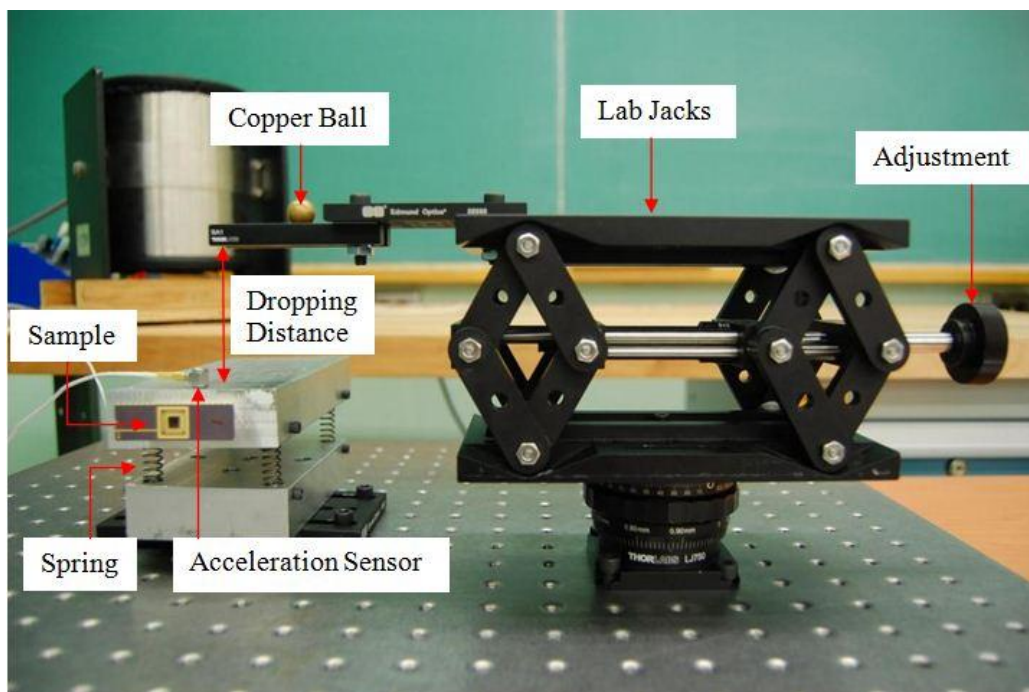
(b)

Figure 3-6: Equipment setup for the test of external force: (a) overview, (b) details of acceleration test system

3.2.1 External force test setup

A prototype which had the structure flipped to the vertical position in previous step was tested in this stage. As show in Figure 3-6, the prototype was attached to the side face of the metal platform, on which an acceleration sensor was located. The acceleration sensor connects to a computer through a data collection card, and then the acceleration subjected by the platform can be read from the computer. Therefore, when a copper ball dropped from a lab jacks to the platform, the acceleration of this ball was read from the output of the sensor on computer. The height of ball was adjusted until the flipped structure dropped under the strike.

3.2.2 Test result and analysis

Test results, as listed in Table 3-1 and Figure 3-7, showed the flipped structure dropped from the vertical position under an acceleration a within the range of 6.25g to 6.38g. The structure dropped at 6.38g, 6.64g and 6.53g in each test. Since the face of the structure was parallel to the platform in this test, its gravity was in the same direction with the acceleration it was subjected. Therefore, the actual maximum acceleration the flipped structure subjected was between 7.25g and 7.38g. Comparing with the acceleration value deduced from simulation result 7.6g, it is acceptable.

Table 3-1: External Force Measurement

Height (cm)	3	4	5	6	7	8	9	10	11	12	13
Data 1 (g)	1.79	2.26	3.16	3.85	4.47	4.88	4.92	5.04	5.66	6.38 (fall)	-
Data 2 (g)	1.37	1.88	2.05	3.36	3.88	4.52	5.15	5.58	6.03	6.64 (fall)	-
Data 3 (g)	1.29	1.72	1.93	2.33	4.42	5.23	5.50	5.66	6.05	6.25	6.53 (fall)

After the flipped structure dropped from the vertical position, it was held by tethers as it shows in Figure 3-4e. The angle between the structure and the substrate is 18.8 ° as measured by Zygo optical interferometer (Figure 3-8), which is consistent with the designed angle 20 °.
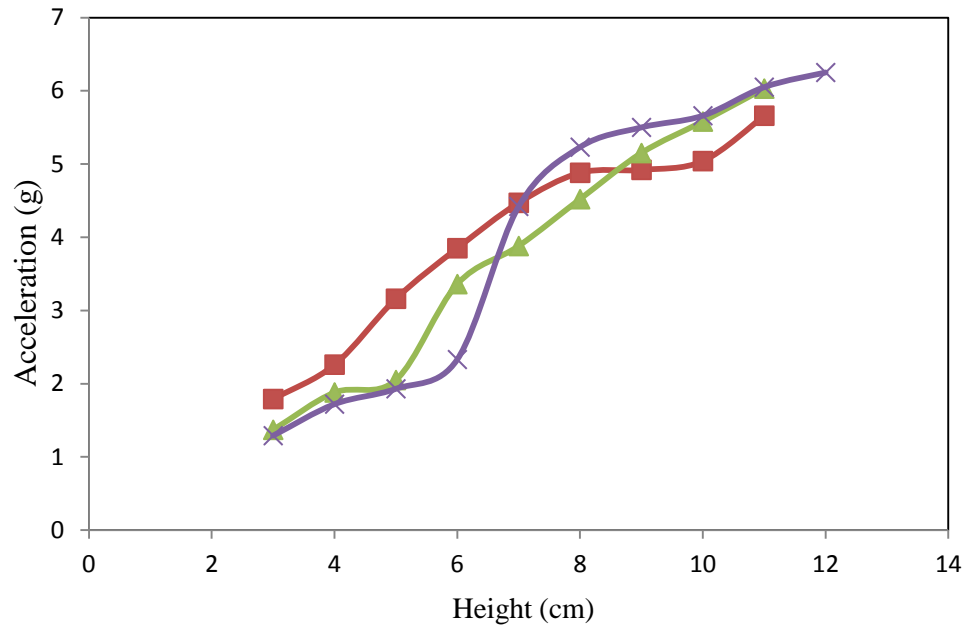
Figure 3-7: External Force Measurement
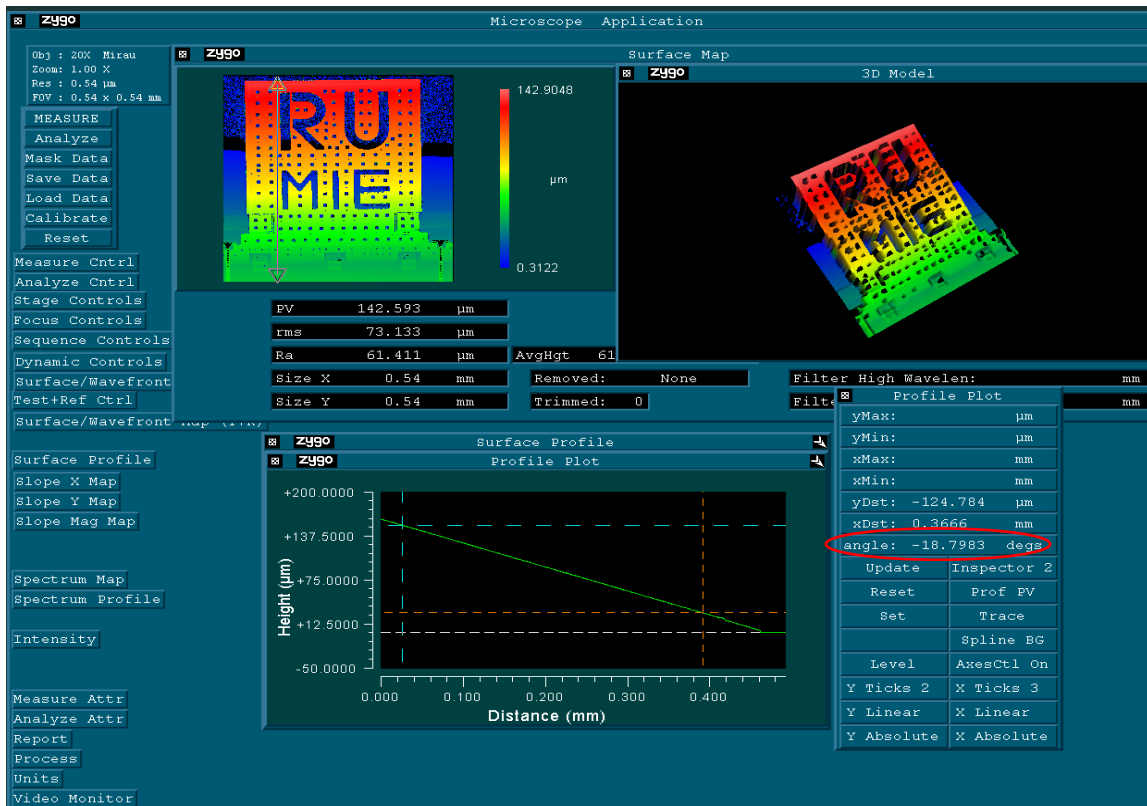
Figure 3-8: Display on Zygo optical interferometer when the structure is held by tether

3.3 Discussion

Some phenomena were observed in the experiment. Firstly, because of the nature of SEM, it was observed in early experiments that the flipped structure was moved by the electric beam in SEM. It can be seen in Figure 3-9 that charges were concentrated on the edges of the structure. To conduct the electricity away, a layer of gold was deposited on the flipped structure of one prototype and connected with a ground wire. In this way, the flipped structure would not affected by the electricity in SEM.
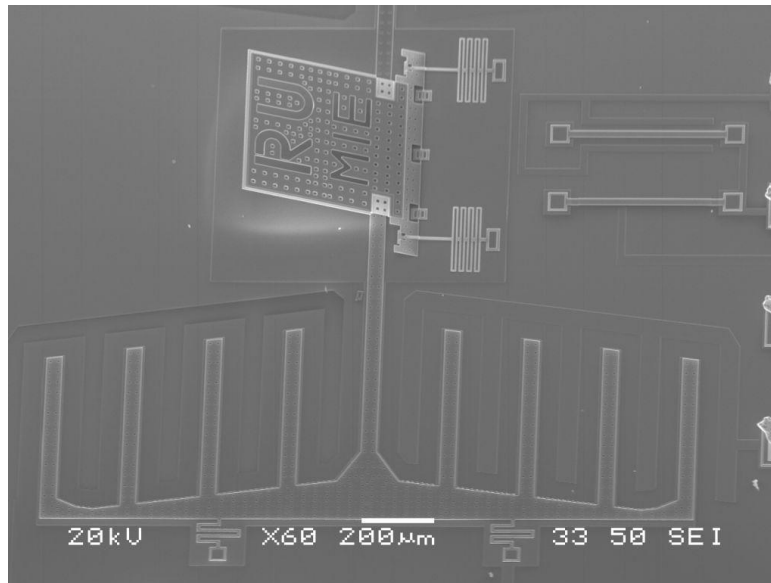
Figure 3-9: Flip-up system without gold layer under SEM

Another problem was the influence that the length of tether on its stiffness. When tethers were short, the flip-up structure could not be lifted by the actuator; or they could bend downward if tethers are long and the external force was too large. As it shows in Figure 3-10, the angle between the structure and substrate became $10.2°$ while the structure was held by tethers. Because the tethers have a large length to thickness ratio, they could not support the structure under a great shock. In this circumstance, the flipped structure would not be locked at the designed angle. Because the numbers of the prototypes was limited and this test was destructive, the magnitude of the force that causes this failure was not able to be tested.
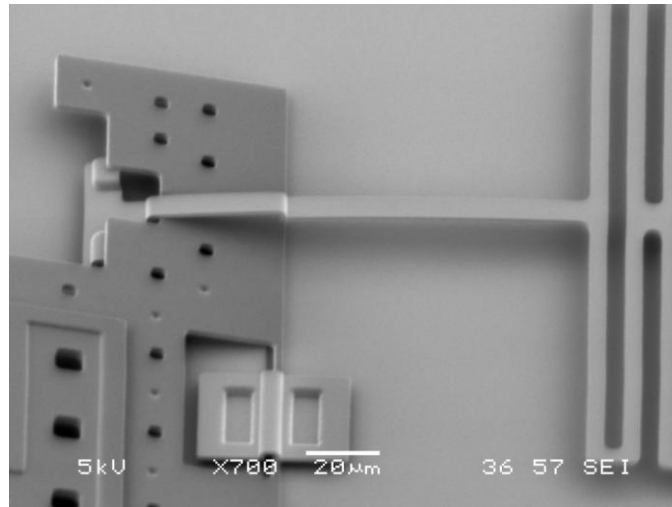
(a)
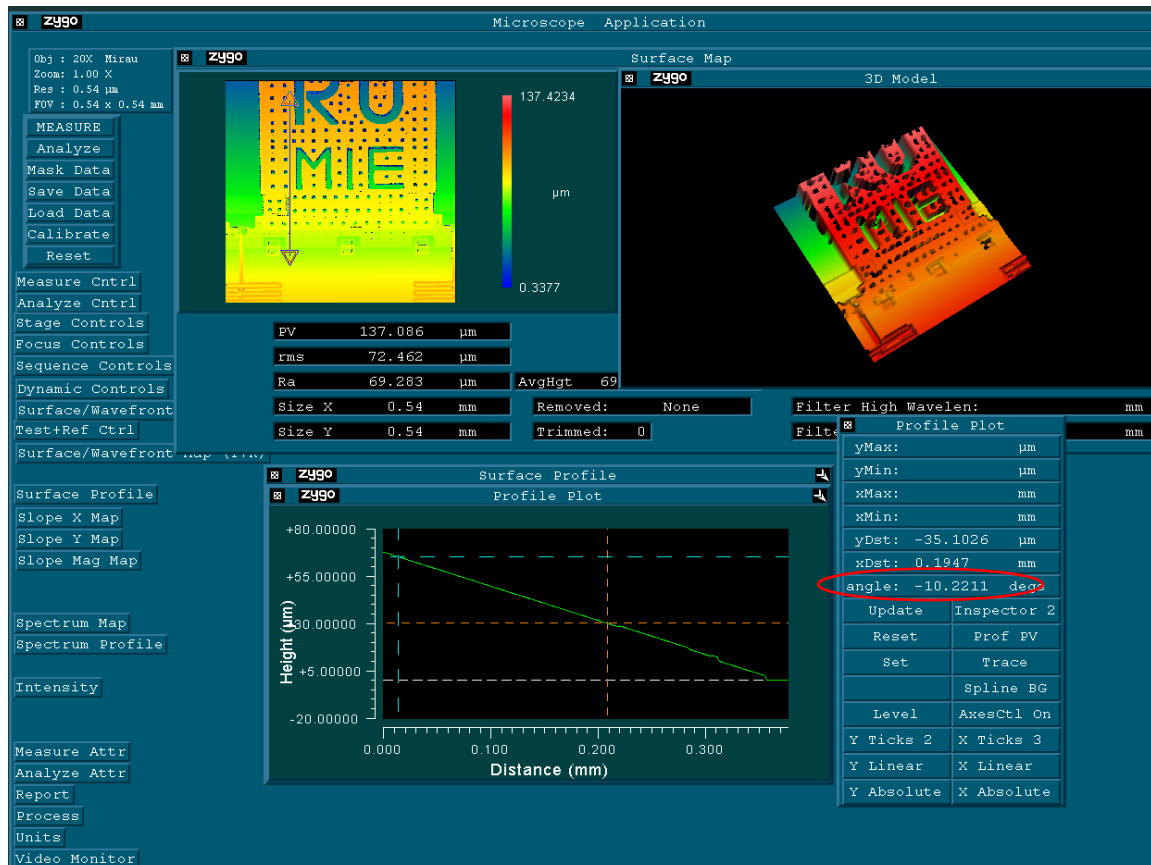
(b)

Figure 3-10: Curved tether (a) SEM image of the curved tether, (b) Display on Zygo optical interferometer when tether bend downward

Chapter 4 Micromirror and applications

With the emergence of optic network in recent years, the application of MEMS technology in network communications has aroused the interest of industry and led to the fast development of a new technology - MOEMS (Micro-opto-electro-mechanical Systems). MOEMS is an important research direction, which integrates micro-optics, microelectronics and micro-mechanics. It brings new opportunities to realize device miniaturization and high performance in optical communication. Micromirrors, as an important optical device with the capability of scanning and beam steering, have found numerous applications in various fields.

4.1 Design of micromirror on pop-up structure

In this thesis, a micromirror is designed on the basis of the flipped structure as illustrated in Figure 4-1. After the flip-up system is assembled by the repulsive-force actuator, the space under the flipped structure increases, so that the micromirror can rotate a large angle within this space driven by parallel-plate actuator. The micromirror can rotate around either one or two axis, under the force provided by one or multiple actuators, as shown in Figure 4-2 and Figure 4-3.

Basing on the working principle, the applications of micromirror can be divided into resonant based and non-resonant based. The resonant based applications, such as barcode scanning, object tracking and positioning and vector display, utilize the fast scanning capability of mirrors. They usually work under resonant frequencies, so resonant frequency is an important parameter for these applications. Some other applications, like variable optical attenuator (VOA), optical switch, and projection display, are not working under resonant frequencies, but have high requirement on the scan angle of mirror. Scan angle and resonant frequency are the main concerns in this design.

In the single-axis design, a micromirror is embedded into the flipped structure connecting by either a serpentine spring (Figure 4-2a) or a beam (Figure 4-2b) on each side. A fixed electrode is located under the upper half of the mirror. After the flipped structure is assembled, it forms an angle with the substrate together with the mirror. When a voltage is applied, the upper mirror is

attracted down to the fixed electrode, which returns to original position under the restoring force of springs or beams when voltage is removed.
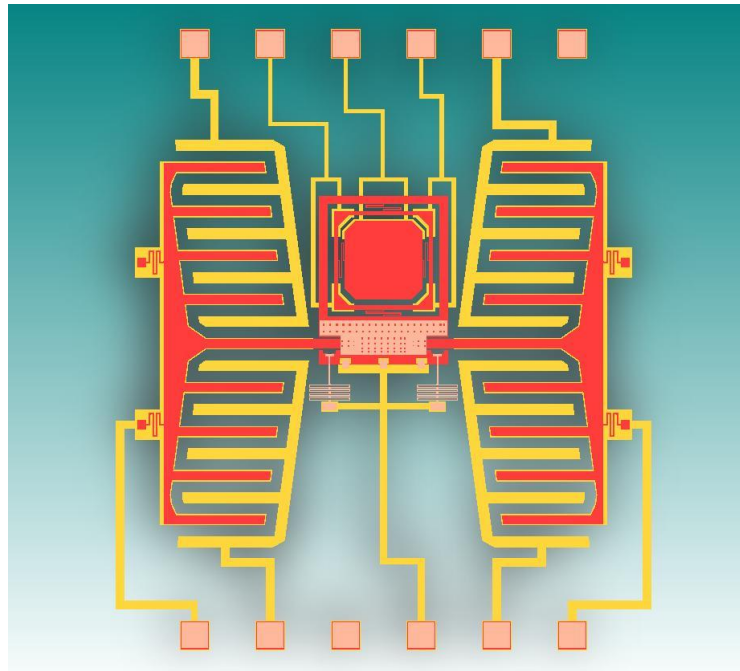
Figure 4-1: Micromirror on pop-up structure

| (a) | (b) |
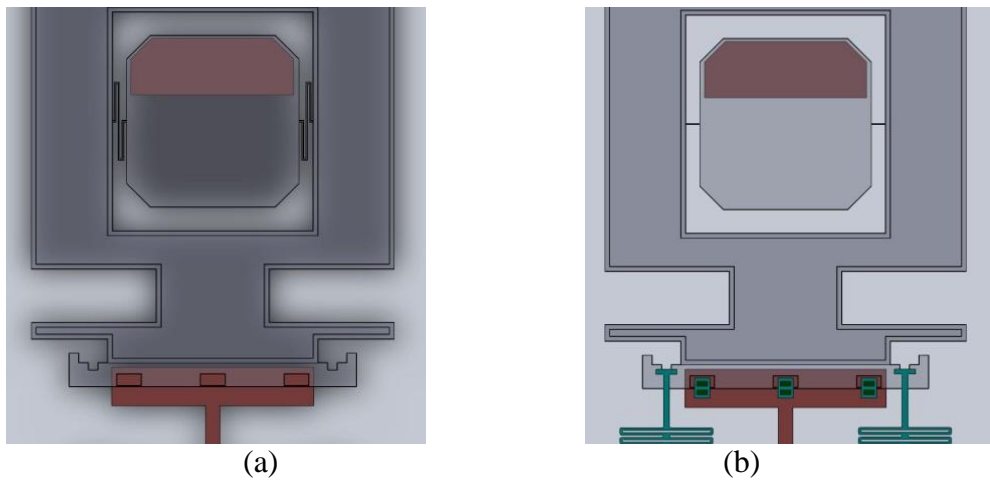
Figure 4-2: Single axis rotating micromirror (a) Single axis rotating micromirror connected by serpentine spring, (b) single axis rotating micromirror connected by beam.

(a)   (b)
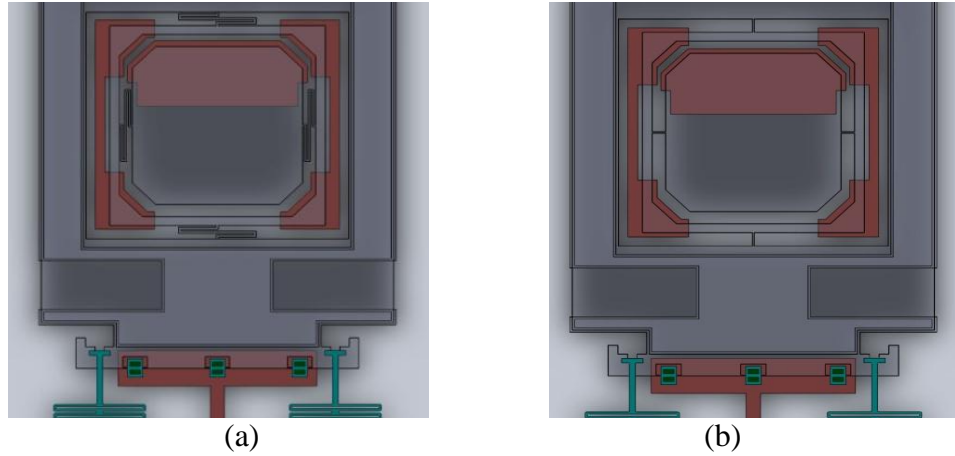
Figure 4-3: Two axis rotating micromirror (a) Two-axis rotating micromirror connected by serpentine spring, (b) two-axis rotating micromirror connected by beam.

In the design with two-axis rotating micromirror, the mirror is connected to a frame and then connected to the flipped structure by serpentine springs (Figure 4-3a) or beams (Figure 4-3b). The frame, as well as the mirror connected to it, tilts bi-directionally by the attraction force from two fixed electrodes under it, when voltage is applied. The mirror also rotates independently to achieve tilting on the second axis.

4.2 Simulation

To obtain the scan angle and resonant frequency of the micromirror on flipped structure, simulations were performed. In the beginning, a 2D graph for each part of the structure was drawn using AutoCAD [58] and saved as .dxf file, which was then imported to Solidworks [59]. In Solidworks, 3D model of each part was constructed by adding thickness element. The individual parts were assembled and the assembled structure was saved in .sat format to import to Coventor [55]. After defining the properties of materials, boundary conditions and voltage range in Coventor, pull-in voltage, displacement and resonant frequency of the structure were precisely calculated. Solidworks drawings showed that the centre of the micromirror was 50.5 μm high to the substrate, when the flipped structure was assembled at 5 °. Therefore, there is sufficient space under the structure for the mirror to rotate. To test the impact of flip-up angle on the performance of micromirror, the flipped structure was assembled at different angles in the following simulations - 5 ° for single-axis rotating micromirrors and 10 ° for two-axis mirrors. In

the simulation, the axis that the frame rotates about is considered as X-axis and the axis that the mirror rotates around is Y-axis.

4.2.1 Single-axis rotating micromirror

Since pull-in phenomenon is a main issue of parallel-plate actuator, pull-in voltages were first tested. In Coventor, when the flipped structure was assembled to 5 °, voltage was added gradually until pull-in effect showed up. For serpentine spring connected single axis mirror, it was at 136.33V; for the beam connected single axis mirror, pull-in phenomenon showed at 149.61V. The voltages applied to each single axis micromirror in the following simulation were no more than its pull-in voltage to ensure its functionality.

As the simulation indicates in Figure 4-4a, the upper edge of the serpentine spring connected micromirror dropped 20.5 μm (Zdown) under the attraction force from fixed electrode under 135V voltage, and the lower edge raised 14.3 μm (Zup). With a total length L of 360 μm, the tilt angle α of micromirror was calculated using Equation 5-1, which was 5.5 °. For the beam connected single-axis micromirror in Figure 4-4b, upper edge dropped 1.4 μm and the lower edge raised 3.4 μm under 145V voltage, so its tile angle was 0.8 °. The changes of tile angle with applied voltage for both types of micromirrors are listed in Table 4-1 and the trends are easily observed in Figure 4-5.

4.2.2 Two-axis rotating micromirror

When the flipped structure was at 10 °, pull-in voltage was tested for two-axis rotating mirror. No pull-in effect was observed until 300V voltage was applied when the mirror rotated around Y-axis. Since the maximum voltage output by the available power generator is 200V, 200V voltage was used in the later simulation for two-axis rotating around Y-axis. And the pull-in voltage was found to be 175V when the mirror rotates about X-axis.

The simulation results of two-axis rotating micromirrors are shown in Figure 4-6 and Figure 4-7. The detailed data are listed in Table 4-2.When the flipped structure was assembled at 10 °, the serpentine spring connected micromirror rotated 1.3 ° along Y-axis under 200V voltage and 7.1 ° along X-axis under 175V voltage. The beam connected micromirror had 0.3 ° tilt angle in Y-axis and 0.8 ° in X-axis.
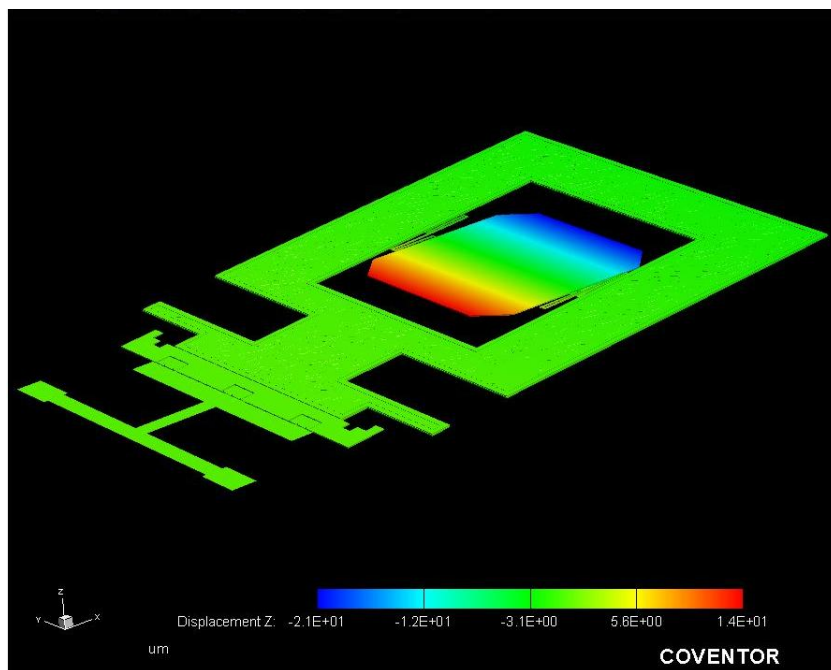
(a)
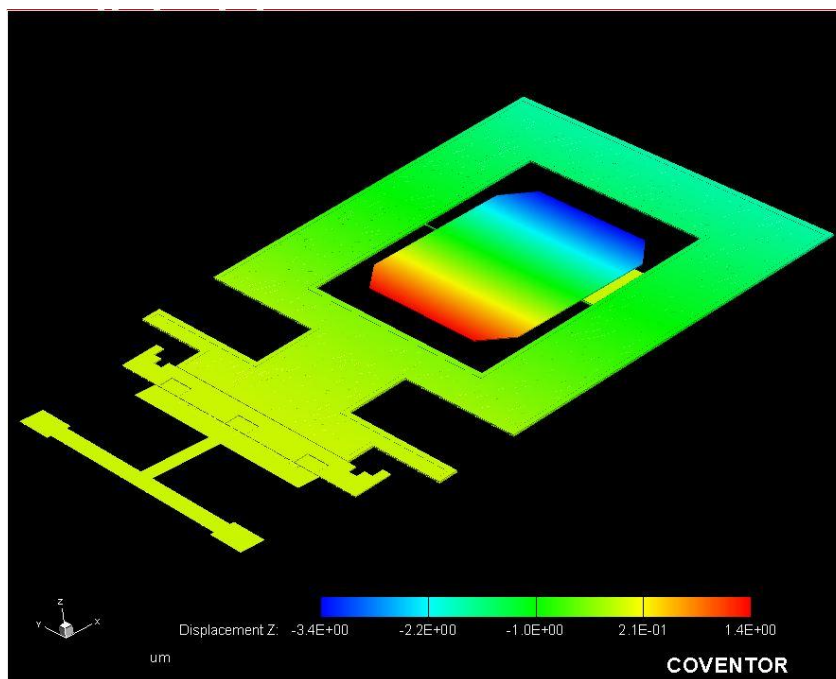
(b)

Figure 4-4: Displacement of single-axis micromirror under 130V voltage in (a) serpentine spring connected system; (b) beam connected system

Table 4-1: Relation of tile angle and applied voltage for single-axis rotating micromirrors

	100V	105V	110V	115V	120V	125V	130V	135V	140V	145V
Beam Connected Micromirror	0.34°	0.38°	0.42°	0.46°	0.51°	0.55°	0.61°	0.66°	0.72°	0.78°
Spring Connected Micromirror	1.93°	2.20°	2.51°	2.86°	3.29°	3.81°	4.44°	5.53°	-	-
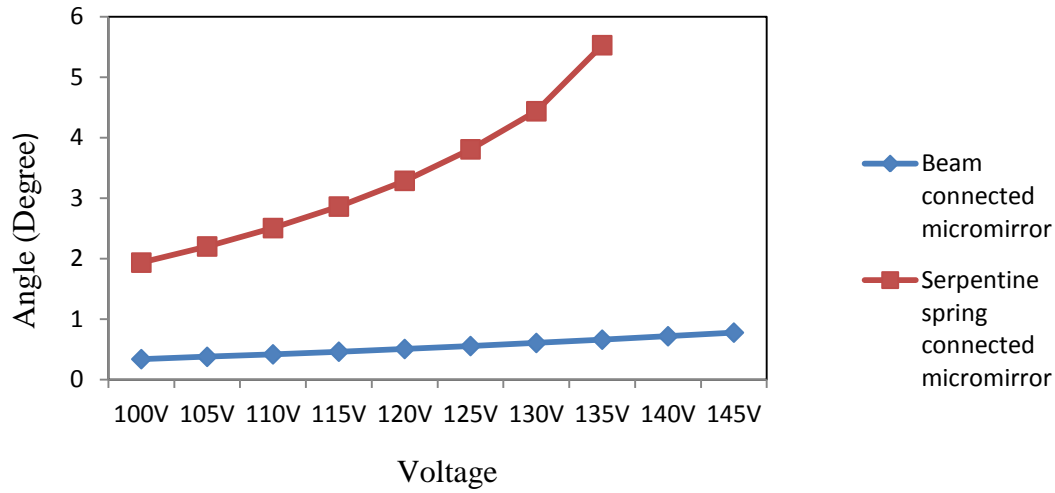
Figure 4-5: Tile angle vs. applied voltage for single-axis rotating micromirrors

$$\alpha = \tan^{-1} \frac{Z_{down} + Z_{up}}{L} \qquad (5\text{-}1)$$

The tile angles in X-direction in the two-axis micromirrors are less than the single-axis ones. It is because the electrodes became farer when the flipped structure assembled at 10°. However, the tile angle can be increased greatly when the micromirror works under resonant frequency. The resonant frequency for serpentine springs connected micromirror was found to be 1797.77Hz in X-axis direction and 3027.71 Hz in Y-axis direction. For beam connected micromirror, resonant frequency was 4593.49Hz in X-axis direction and 6560.22Hz in Y-axis direction.

55

Table 4-2: Properties of two-axis rotating micromirrors assembled at 10 °

		Resonant Frequency (Hz)	Tile Angle
Beam Connected Micromirror	X-axis	4593.49	0.8 °
	Y-axis	6560.22	0.3 °
Spring Connected Micromirror	X-axis	1797.77	7.1 °
	Y-axis	3027.71	1.3 °

4.3 Discussion

In above designs, micromirror works under the combined action of repulsive-force actuator and parallel-plate actuator. The combination of two actuators brings advantages: repulsive-force actuator assembles the flipped structure at an angle with the substrate, so that provides more space for the micromirror to rotate; comparing with other types of actuators, electrostatic actuators can achieve fast and precise position [44].

Serpentine springs and beams were used to connect mirror, frame and the flipped structure in the simulation. Box spring was not adopted in the design, since it has a similar effect with beam under torsion. Because of the low rigidity of serpentine spring, the mirror system connected by it has a larger tilt angle than the beam connected systems under the same voltage. However, the shape of serpentine spring leads to the movement of rotating axis under the attraction from electrodes. While for the beam connected system, it can be guaranteed that the rotation of mircromirror is around the beam at its central axis.

On the other hand, when a voltage was applied, not only the corresponding parts above the electrodes were pulled down, but the whole mirror, frame and structure were under the attraction force. And the attraction force increases with the increasing of applied voltage. For single-axis rotating micromirrors, the flipped structure was in 5 ° with the substrate, so the attraction force was relatively large. To resist this attraction, the structure area around the micromirror was increased. The flipped structure has two layers – Poly1 and Poly2, so it is harder to be pulled down by the electrostatic force. For the two-axis micromirrors, the flipped structure was assembled at 10 °. The structure, frame and mirror were farer to the electrode, so the attraction force was not significant. Furthermore, the two-axis rotating micromirror usually works under

resonant frequency, for example, as a projection display. At this time, the voltage is low, then the attraction on the structure can be neglected.
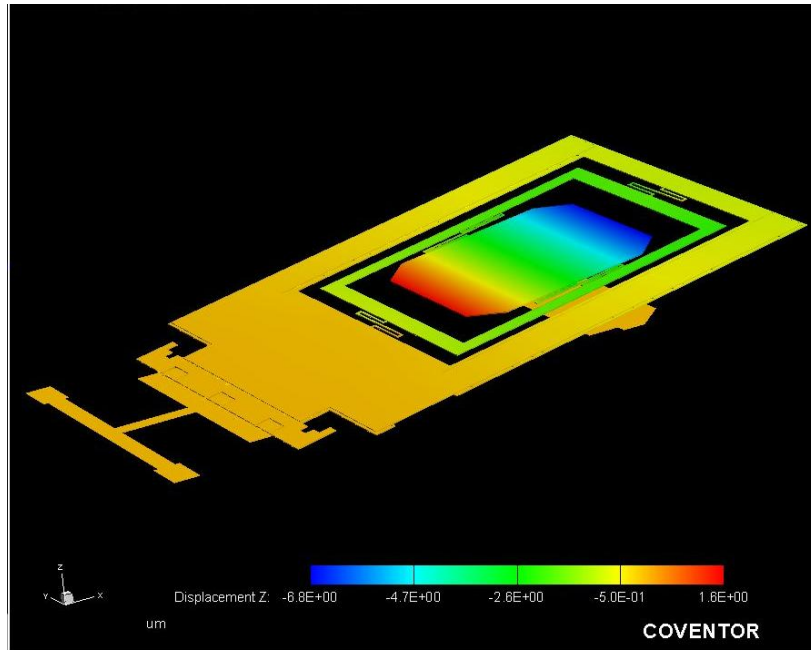
(a)
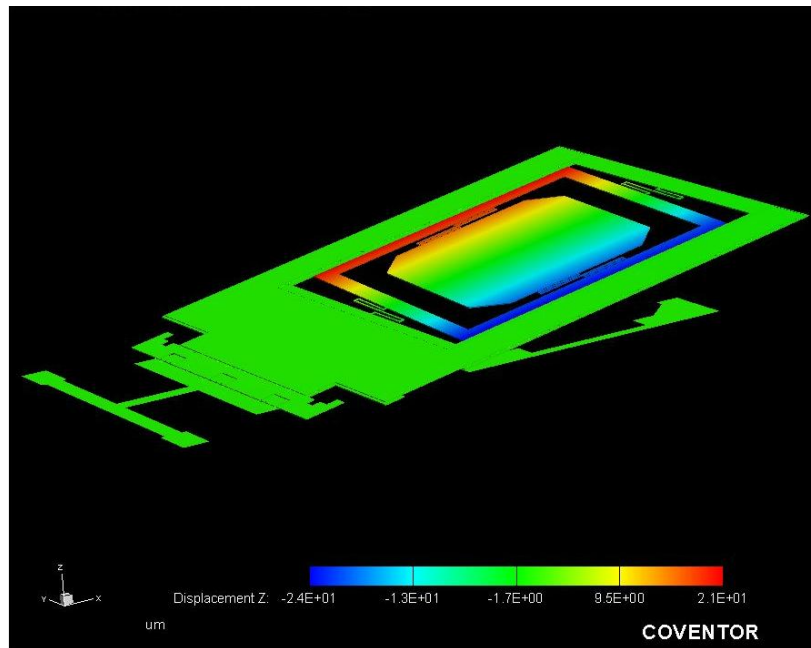
(b)

Figure 4-6: Displacement of two-axis serpentine spring connected micromirror under 200V voltage when rotating along (a) Y-axis, (b) X-axis

(a)
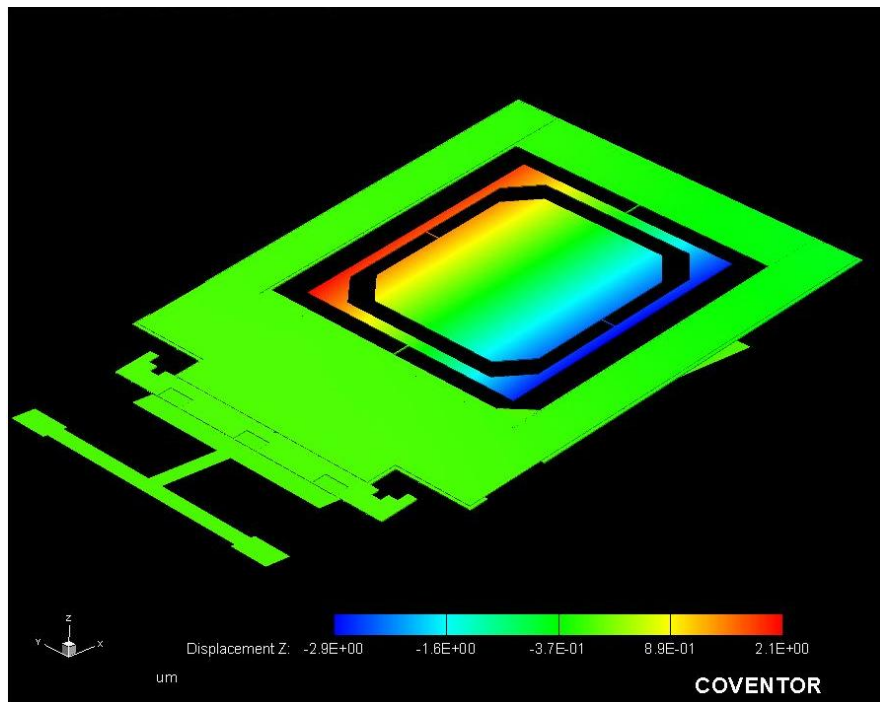
(b)

Figure 4-7: Displacement of two-axis beam connected micromirror under 200V voltage when rotating along (a) Y-axis, (b) X-axis

4.4 Applications of micromirror on pop-up structure

4.4.1 Non-resonant type applications

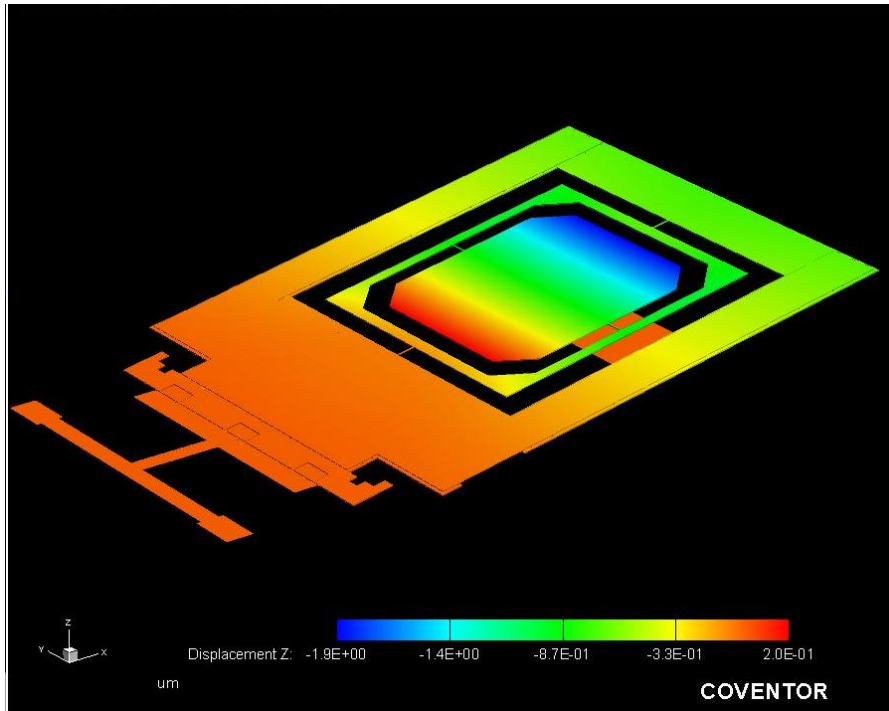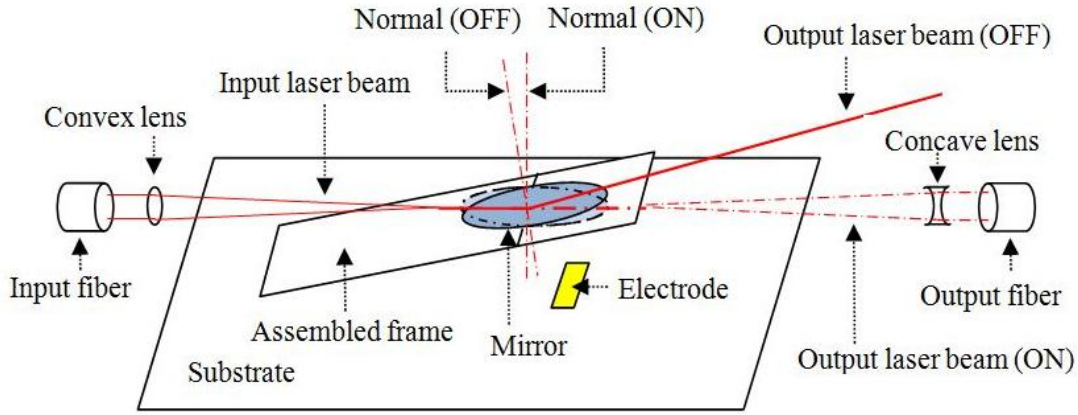Figure 4-8: Single-axis rotating micromirror based optical switch

An optical switch is configured as shown in Figure 4-8. A serpentine spring connected single-axis rotating micromirror is applied. Though the rotating axis can move during the rotation of micromirror, it does not affect the operation of optical switch. Furthermore, the large tile angle of this design helps in this situation. The input and output fibers are arranged in a plane horizontal to the substrate, with the flipped structure between them. The laser beam from the input fiber goes through a convex lens and focuses on the mirror. When the mirror is in its original position, the beam is steered toward the out-of-plane direction, so the switch is at the OFF position. When the voltage is applied on the electrode underneath the upper half of the mirror, this half of mirror is attracted down. The mirror rotates to a position, so that the input beam transmits above the mirror and reaches the output fiber, which is the ON state of the switch. The mirror can also tilt in two axes and be used in 3D switches shown in Figure 1-17 and Figure 1-18.

Similar with the principle it works in optical switch, the serpentine spring connected single-axis rotating micromirror is also applied in VOA (Figure 4-9). When the parallel-plate actuator is power off, the VOA is in OFF state that the input laser beam leaves without being interfered. By changing the applied voltage on the actuator, the mirror rotates around the axis. The quantity of reflected laser beam and attenuation of signal also changes accordingly.
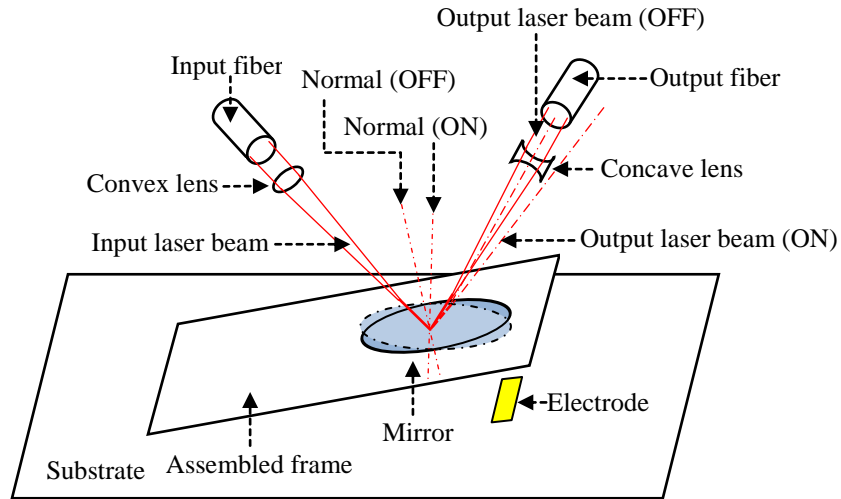
Figure 4-9: Single-axis rotating micromirror based VOA

4.4.2 Resonant-based applications

Figure 4-10 shows a projection display design basing on two-axis rotating micromirror. Comparing with large scan angle, high speed and precise positioning is more important to the applications, therefore the beam connected two-axis rotating micromirror is used here. The input beam is reflected by the micromirror and then projected on the screen. With the rotation of mirror, the beam scans bidirectional along x-axis. Also the tilt of frame leads to the movement of beam in the y-axis. Therefore, a bidirectional raster scan is able to be achieved by this system.
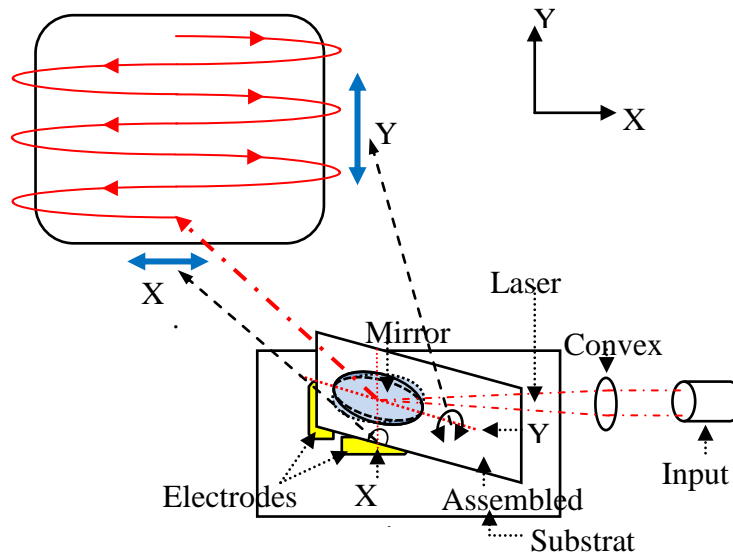
Figure 4-10: Two-axis rotating micromirror based projection display

Chapter 5 Conclusion

5.1 Contributions

- Developed a novel automated micro assembly mechanism.

  This mechanism consists of two rotational repulsive-force microactuators, hinges, two tethers and the flipping structure. The structure is flipped up after obtaining an initial velocity from the action of repulsive-force actuators. The micro assembly mechanism can realize assembly of micro structures not only at the vertical position (perpendicular to the substrate) but also at positions at any angle to the substrate. This automated assembly mechanism has three advantages: 1) Need no external interference; 2) Wafer-level multi-devices batch assembly; and 3) Suitable for matured commercial surface micromachining process such as PolyMUMPs.

- Both a graphical and an analytical approach are developed for designing the novel micro assembly mechanism.

- Prototypes were fabricated and tested. Experimental results verified the concept of the novel automated micro assembly mechanism.

- The strength of the assembled 3D structures in terms of withstanding external acceleration is calculated. The calculated result well matches the experimental result which is about 7.6g.

- Using the micro assembly mechanism, 1D and 2D rotation micromirrors are designed for various applications.

5.2 Future Work

It is observed in the experiment that tethers could bend under a large force, so that the flipped structure cannot be held at the designed assembly angle. To amend this issue, the rigidity of tethers need be increased. Since its thickness is fixed, the modification can only be shortening the tethers or increasing the distance between lower notches to the rotating axis. However, tethers cannot be too short, since their high stiffness will make the structure hard to be lifted. Therefore, the relation between the driving force of actuator and the stiffness of tethers will be examined.

On the other hand, single-axis and two-axis rotating micromirrors were designed and simulated in this thesis. They will be fabricated and tested in the future.

References

[1] MEMSnet. http://www.memsnet.org/mems/what_is.html.

[2] S. A. Vittorio. MicroElectroMechanical Systems (MEMS). http://www.csa.com/discoveryguides/mems/overview.php.

[3] S. He. Microelectromechanical Systms Lecture Notes. Winter 2010.

[4] Embedded Energy. Cymbet Corporation. http://www.cymbet.com/content/products-embedded-energy.asp.

[5] S. K. Nayar and V. Branzo, Programmable Imaging: Micro-Mirror Arrays, Columbia University. http://www.cs.columbia.edu/CAVE/projects/pi_micro/pi_micro.php.

[6] Thermal Actuators, Sandia National Laboratories. http://www.mems.sandia.gov/about/actuators.html.

[7] M. Ming and C. Lee, Tunable Coupling Regimes of Silicon Microdisk, Optics Express, Vol. 14, pp. 4703-4712, May 2006.

[8] M. G. Lee and J. Kim, A Discrete Positioning Microactuator: Linearity Modeling and VOA Application, Journal of Microelectromechanical Systems, Vol. 16, pp. 16-23, February 2007.

[9] M. Hill, 'Seesaw' Switch is First Practical Micro-Electro-Mechanical Optical Switch, Alcatel Lucent. http://www.bell-labs.com/news/1999/february/23/1.html.

[10] G. T. A. Kovacs, N. I. Maluf, and K. E. Petersen, Bulk Micromachining of Silicon, Proceedings of the IEEE, Vol. 86, pp. 1536 - 1551, 1998.

[11] J. M. Bustillo, R. T. Howe, and R. S. Muller, Surface Micromachining for Microelectromechanical Systems, Proceedings of the IEEE, Vol. 86, pp. 1552 - 1574, 1998.

[12] N. Dechev, M. Basha, S. K. Chaudhuri, and S. Safavi-Naeini, Microassembly of 3D Micromirrors as Building Elements for Optical MEMS Switching, Proceedings of the SPIE, pp. 63760C, 2006.

[13] R. Murthy, A. Das and D. O. Popa, ARRIpede: An Assembled Micro Crawler, 8th IEEE Conference on Nanotechnology, pp. 833 – 836, Aug 2008.

[14] Y. Chiu, W. Huang, J. Wu, J. Chiou, and H. D. Shieh, Assembly of Micro Mirrors on SOI Wafers Using SU-8 Mechanisms and One-Push Operation, 2008 IEEE/LEOS Internationall Conference on Optical MEMs and Nanophotonics, pp. 11, Aug 2008.

[15] S. Oak, G. F. Edmiston, G. Sivakumar, and T. Dallas, Rotating Out-of-Plane Micromirror, Journal of Microelectromechanical Systems, Vol. 19, pp. 632-639, June 2010.

[16] E. E. Hui, R. T. Howe, and M. S. Rodgers, Single-Step Assembly Of Complex 3-D Microstructures, In Proceeding of 13th IEEE International Micro Electro Mechanical Systems Conference, pp. 602-607, January 2000.

[17] H. K. Chu, J. K. Mills, and W. L. Cleghorn, Parallel Microassembly with a Robotic Manipulation System, Journal of Micromechanics and Microengineering, Vol. 20, pp. 125027, 2010.

[18] S. H. Tsang, D. Sameoto, I. G. Foulds, R. WJohnstone, and M. Parameswaran, Automated Assembly of Hingeless 90◦ out-of-plane Microstructures, Journal of Micromechanics and Microengineering, pp. 1314–1325, 2007.

[19] K. W. C. Lai, A. P. Hui, and W. J. Li, Non-Contact Batch Micro-Assembly by Centrifugal Force, Proceeding of the 15th IEEE 2004 International Conference on MEMS, pp. 184-187, 2002.

[20] K. W. C. Lai, P..S. Chung, M. Li, and W. J. Li, Automated Micro-Assembly of Surface MEMS Mirrors by Centrifugal Force, Proceedings of 2004 International Conference on Intelligent Mechatronics and Automation, pp. 23 – 28, Aug. 26-31, 2004.

[21] E. Iwase and I. Shimoyama, Multistep Sequential Batch Assembly of Three-Dimensional Ferromagnetic Microstructures With Elastic Hinges, Journal of Microelectromechianical Systems, Vol. 14. No. 6, pp. 1265-1271, 2005.

[22] F. Iker, N. Andre, T. Pardoen, and J. Raskin, Three-Dimensional Self-Assembled Sensors in Thin-Film SOI Technology, Journal of Microelectromechanical Systems, Vol. 15. No. 6, pp. 1687-1697, December 2006.

[23] V. Kaajakari and A. Lal, Thermokinetic Actuation for Batch Assembly of Microscale Hinged Structures, Journal Of Microelectromechanical Systems, Vol. 12, pp. 425-432, August 2003.

[24] V. Kaajakari and A. Lal, Electrostatic Batch Assembly of Surface MEMS Using Ultrasonic Triboelectricity, The 14th IEEE International Conference on Micro Electro Mechanical Systems, pp. 10-13, 2001.

[25] S. Ardanuc, A. Lal, and D. Reyes, Process-Independent, Ultrasound-Enhanced, Electrostatic Batch Assembly, Solid-State Sensors, Actuators and Microsystems Conference, pp. 407 – 410, 2007.

[26] C. J. Morris, H. Ho, and B. A. Parviz, Liquid Polymer Deposition on Free-Standing Microfabricated Parts for Self-Assembly, Journal of Microelectromechanical Systems, Vol. 15, pp. 1795-1804, December 2006.

[27] H. Onoe, K. Matsumoto, and I. Shimoyama, Three-Dimensional Micro-Self-Assembly Using Hydrophobic Interaction Controlled by Self-Assembled Monolayers, Journal of Microelectromechanics Systems, Vol. 13, pp. 603-611, 2004.

[28] A. Winkleman, L. S. McCarty, T. Zhu, D. B. Weibel, Z. Suo, and G. M. Whitesides, Templated Self-Assembly Over Patterned Electrodes by an Applied Electric Field: Geometric Constraints and Diversity of Materials, Journal of Microelectromechanical Systems, pp. 900 - 910, August 2008.

[29] J. Robert Reid, Victor M. Bright, and J.H. Comtois, Automated Assembly of Flip-Up Micromirrors, 1997 International Conference on Solid-state Sensors and Actuators, pp. 347 – 350, June 16-19, 1997.

[30] J. Qiu, J. H. Lang, and A. H. Slocum, A Bulk-micromachined Bistable Relay with U-shaped Thermal Actuarors, Journal of Microelectromechanical Systems, Vol. 14, pp. 1099-1109, 2005.

[31] L. Que, J. Park, and Y. B. Gianchandani, Bent-Beam Electrothermal Actuators—Part I: Single Beam and Cascaded Devices, Journal of Microelctromechanical Systems, Vol. 10, pp. 247 - 254, June 2001.

[32] T. Akiyama, D. Collard, and H. Fujita, Scratch Drive Actuator with Mechanical Links for Self-Assembly of Three-Dimensional MEMS. Journal of Microelectromechanical Systems, Vol. 6, No. 1, pp. 10-17, March 1997.

[33] D. Bayat, C. Ataman, B. Guldimann, S. Lani, W. Noell, and N. F. de Rooij, Large Electrostatically and Electromagnetically Actuated Mirror System for Space Applications, 2010 International Conference on Optical MEMS & Nano photonics, pp. 193 – 194, 2010.

[34] K. Fan, W. Lin, L. Chang, S. Chen, T. Chung, and Y. Yang, A 2x2 Mechanical Optical Switch With a Thin MEMS Mirror, Journal of Light wave Technology, Vol. 27, pp. 1155-1161, May 2009.

[35] C. Ji, Y. Yee, J. Choi, S. Kim, and J. Bu, Electromagnetic 2x2 MEMS Optical Switch, IEEE Journal of Selected Topics in Quantum Electronics, Vol. 10, pp. 545-550, 2004.

[36] Z. Shen and J. Huang, Latching Micromagnetic Optical Switch, Journal of Microelectromechanical Systems, Vol. 15, pp. 16-23, February 2006.

[37] S. D. Robinson, MEMS Technology -- Micromachines Enabling the "All Optical Network". Proceedings of 51st Electronic Components and Technology Conference, pp. 423 – 428, 2001.

[38] J. J. Bernstein, W. P. Taylor, J. D. Brazzle, C. J. Corcoran, G. Kirkos, J. E. Odhner, A. Pareek, M. Waelti, and M. Zai. Electromagnetically Actuated Mirror Arrays for Use in 3-D Optical Switching Application. Journal of Microelectromechanical Systems, pp. 526-535, 2003.

[39] M. Mizukami, J. Yamaguchi, N. Nemoto, Y. Kawajiri, H. Hirata M. Mizukami, J. Yamaguchi, N. Nemoto, Y. Kawajiri, H. Hirata, S. Uchiyama, M. Makihara, T. Sakata, N. Shimoyama, H. Ishii, and F. Shimokawa, 128X128 3D-MEMS Optical Switch Mmodule with Simultaneous Optical Paths Connection for Optical Cross-connect System, International Conference on Photonics in Switching, pp. 1-2, 2009.

[40] K. Isamoto, K. Kato, A. Morosawa, C. Chong, H. Fujita, and H. Toshiyoshi, A 5-V Operated MEMS Variable Optical Attenuator by SOI Bulk Micromachining, IEEE Journal of Selected Topics in Quantum Electronics, Vol. 10, pp. 570-578, August 2004.

[41] D. Dudley, W. Duncan, and J. Slaughter. Emerging Digital Micromirror Device (DMD) Applications. http://focus.ti.com/pdfs/dlpdmd/152_NewApps_paper_copyright.pdf.

[42] M. Kiang, O. Solgaard, K. Y. Lau, and R. S. Muller. Electrostatic Combdrive-Actuated Micromirrors for Laser-Beam Scanning and Positioning. Journal of Microelectromechanical Systems, Vol. 7, pp. 27-37, March 1998.

[43] D. Elata, V. Leus, A. Hirshberg, O. Salomon, and M. Naftali, A Novel Tilting Micromirror with a Triangular Waveform Resonance Response and an Adjustable Resonance Frequency for Raster Scanning Applications, The 14th International Conference on Solid-State Sensors, Actuators and Microsystems, France, pp. 1509 – 1512, 2007.

[44] V. Milanovic and W. K. Lo, Fast and High-Precision 3D Tracking and Position Measurement with MEMS Micromirrors, 2008 IEEE/LEOS Optical MEMS and Their Applications Conference, Germany, pp. 73-73, August 2008.

[45] MUMPs®. http://www.memscap.com/en_mumps.html.

[46] SUMMiT VTM Overview. http://mems.sandia.gov/tech-info/summit-v.html.

[47] Microgem™. http://www.micralyne.com/capabilities/products/micragem.html.

[48] Process Technologies Overview. http://www.jazzsemi.com/process_technologies/overview.shtml.

[49] J. Carter, A. Cowen, B. Hardy, R. Mahadevan, M. Stonefield, and S. Wilcenski, MUMPS design handbook revision 11.0, MEMSCAP Inc.

[50] S. He, R. B. Mrad, and J. Chong, Repulsive-Force Out-of-Plane Large Stroke Translation Micro Electrostatic Actuator, Journal of Microelectromechanical Systems, Vol. 17, No. 7, pp. 532, 2011.

[51] S. He and R. B. Mrad, Large-Stroke Microelectrostatic Actuators for Vertical Translation of Micromirrors Used in Adaptive Optics, IEEE Transactions on Industrial Electronics, Vol. 52, pp. 974 – 983, August 2005.

[52] S. He and R. B. Mrad, Design, Modeling, and Demonstration of a MEMS Repulsive-Force Out-of-Plane Electrostatic Micro Actuator, Journal of Microelectromechanical Systems, Vol. 17, pp. 532-547, June 2008.

[53] R. W. Johnstone. Automated Design for Micromachining. http://www.sfu.ca/adm/index.html.

[54] K. S. J. Pister, M. W. Judy, S. R. Burgett, and R. S. Fearing, Microfabricated Hinges, Sensors and Actuators A: Physical, Vol. 33, pp. 249-256, 1992.

[55] CoventorWare®. http://www.coventor.com/coventorware.html.

[56] J. Liu, L. Fan, and D. L. DeVoe, Microfabricated Sequential-Leaf Time-Delay Mechanisms, Journal of Microelctromechanical Systems, Vol. 14, pp. 1051-1060, October 2005.

[57] CMC Microsystems. http://www.cmc.ca/.

[58] Autodesk - 3D Design & Engineering Software for Architecture, Manufacturing, and Entertainment. http://www.autodesk.com/.

[59] 3D CAD Design Software Solidworks. http://www.solidworks.com/.